Physics of Plasmas

Validation of gyrokinetic simulations in NSTX and projections for high-k turbulence measurements in NSTX-U

Cite as: Phys. Plasmas **27**, 122505 (2020); https://doi.org/10.1063/5.0009620
Submitted: 01 April 2020 . Accepted: 03 November 2020 . Published Online: 08 December 2020

J. Ruiz Ruiz, W. Guttenfelder, A. E. White, N. T. Howard, J. Candy, Y. Ren, D. R. Smith, N. F. Loureiro, C. Holland, and C. W. Domier

COLLECTIONS

Paper published as part of the special topic on Papers from the 61st Annual Meeting of the APS Division of Plasma Physics

View Online Export Citation CrossMark

ARTICLES YOU MAY BE INTERESTED IN

Internal measurement of magnetic turbulence in ELMy H-mode tokamak plasmas
Physics of Plasmas **27**, 120701 (2020); https://doi.org/10.1063/5.0029996

Blob interactions in 2D scrape-off layer simulations
Physics of Plasmas **27**, 122301 (2020); https://doi.org/10.1063/5.0021314

Modeling of resistive plasma response in toroidal geometry using an asymptotic matching approach
Physics of Plasmas **27**, 122503 (2020); https://doi.org/10.1063/5.0020010

AIP Publishing Physics of Plasmas Features in Plasma Physics Webinars Register Today!

AIP Publishing

© 2020 Author(s).

Physics of Plasmas ARTICLE scitation.org/journal/php

Validation of gyrokinetic simulations in NSTX and projections for high-k turbulence measurements in NSTX-U

Cite as: Phys. Plasmas **27**, 122505 (2020); doi: 10.1063/5.0009620
Submitted: 1 April 2020 · Accepted: 3 November 2020 ·
Published Online: 8 December 2020

J. Ruiz Ruiz,[1,2,a),b)] W. Guttenfelder,[3] A. E. White,[2] N. T. Howard,[2] J. Candy,[4] Y. Ren,[3] D. R. Smith,[5] N. F. Loureiro,[2] C. Holland,[6] and C. W. Domier[7]

AFFILIATIONS

[1]Rudolf Peierls Centre for Theoretical Physics, University of Oxford, Oxford OX1 3NP, United Kingdom
[2]Massachusetts Institute of Technology (MIT), Cambridge, Massachusetts 02139, USA
[3]Princeton Plasma Physics Laboratory, Princeton, New Jersey 08543, USA
[4]General Atomics, P.O. Box 85608, San Diego, California 92186, USA
[5]University of Wisconsin-Madison, Madison, Wisconsin 53706, USA
[6]Center for Energy Research, University of California-San Diego (UCSD), La Jolla, California 92093-0417, USA
[7]University of California at Davis, Davis, California 95616, USA

Note: This paper is part of the Special Collection: Papers from the 61st Annual Meeting of the APS Division of Plasma Physics.
Note: Paper TI2 1, Bull. Am. Phys. Soc. 64 (2019).
[a)]Invited speaker.
[b)]**Author to whom correspondence should be addressed:** juan.ruiz@physics.ox.ac.uk

ABSTRACT

An extensive validation effort performed for a modest-beta NSTX NBI-heated H-mode discharge predicts that electron thermal transport can be entirely explained by electron-scale turbulence fluctuations driven by the electron temperature gradient mode (ETG), both in conditions of strong and weak ETG turbulence drive. Thermal power-balance estimates computed by TRANSP as well as the shape of the high-k density fluctuation wavenumber spectrum and the fluctuation level ratio between strongly driven and weakly driven ETG-turbulence conditions can be matched by nonlinear gyrokinetic simulations and a synthetic diagnostic for high-k scattering. Linear gyrokinetic simulations suggest that the ion-scale instability in the weak ETG condition is close to the critical threshold for the kinetic ballooning mode instability, and nonlinear ion-scale gyrokinetic simulations show that turbulence might be in a state reminiscent of a Dimits' shift regime, opening speculation on the role that ion-scale turbulence might play for the weak ETG condition. A simulation that matched all experimental constraints is chosen to project high-k turbulence spectra in NSTX-U, revealing that the new high-k system [R. Barchfeld *et al.*, Rev. Sci. Instrum. **89**, 10C114 (2018)] should be sensitive to density fluctuations from radially elongated streamer structures. Two schemes are designed to characterize the radial and poloidal wavenumber dependence of the density fluctuation wavenumber power spectrum around the streamer peak, suggesting future high-k fluctuation measurements could be sensitive to an asymmetry in the k_r spectrum introduced due to the presence of strong background flow shear.

Published under license by AIP Publishing. https://doi.org/10.1063/5.0009620

I. INTRODUCTION

Micro-turbulence is believed to be responsible for the anomalous transport of particles, energy, and momentum across the confining magnetic field in fusion plasma experiments. In the core of conventional tokamaks, micro-instabilities can be driven at ion gyro-radius scales ($k_\perp \rho_s < 1$), such as the ion temperature gradient mode (ITG[1]) and trapped electron mode (TEM[2]), and at electron scales ($k_\perp \rho_s > 1$) such as the electron temperature gradient (ETG) mode.[3–6] These micro-instabilities can ultimately develop into turbulence and drive so-called *anomalous* transport that can largely exceed predictions from neoclassical collisional theory.[7] Here $k_\perp$ is the wavenumber of the turbulence perpendicular to the confining magnetic field, and

$\rho_s = c_s/\Omega_{c,i}$ is the ion-sound gyro radius evaluated at the ion sound speed $c_s = \sqrt{T_e/m_i}$, and $\Omega_{c,i} = eB/m_i$ is the ion gyro-frequency.

Analysis of micro-stabilities in the core of spherical tokamak (ST) plasmas, mainly NSTX[8] and MAST,[9] has shown that a number of additional instabilities to the well-known ITG/TEM/ETG can become unstable and drive anomalous electron thermal transport. These can be represented in regime plots showing the dominant linear instability depending on the parametric regime of operation. In Figs. 1(a)–1(c), the regime plots schematically show the dominant linear instability present in various NSTX H-modes at $r/a \sim 0.6\ -0.7$ using the gyrokinetic code GYRO,[10] vs local parameters (Fig. 1 is courtesy of Guttenfelder[11]). The traditional electrostatic ITG/TEM/ETG instabilities are most unstable at rather low values of electron beta β_e. In conditions when the ion-scale instability is suppressed, ETG can now be the main driver of anomalous electron thermal transport at low β_e and normalized electron temperature $a/L_{\rm Te}$ exceeding the critical temperature gradient $a/L_{\rm Te,crit}$,[12] as will be supported in this article. The micro-tearing mode (MT[13–15]) can become unstable at high collisionality $\nu^{e/i}$ and high β_e, while the kinetic ballooning mode (KBM[16]) is predicted to be unstable at lower collisionality and high β_e and high $\alpha_{\rm MHD}$ (MHD α parameter). The reader is referred to Ref. 11 for precise definitions and normalizations.

The present article focuses on NSTX H-mode 141767, which has been extensively analyzed in Refs. 17–20. A total of 2 MW of NBI heating was used to heat the plasma in the time of interest (no RF heating), producing toroidal rotation levels of characteristic Mach number $M \sim 0.2$. Line-integrated density $\langle n_e \rangle \sim 6 \times 10^{15}\ {\rm cm}^{-2}$ and toroidal magnetic field $B_T \sim 0.5$ T on the magnetic axis, while MHD activity was quite low (total toroidal beta $\beta_T^{\rm TOT} \sim 5\% - 6\%$). The plasma current was purposely ramped down from $I_p \approx 1.1 \rightarrow 0.9$ MA, separating strongly driven and weakly driven ETG turbulence regimes at $r/a \sim 0.7$ as measured via high-k scattering.[21] The experimental profile values at $r/a \sim 0.7$ are mapped into regime plots in Fig. 1 for both the strong and weak ETG conditions (blue and green stars), suggesting that the KBM and the micro-tearing mode are expected to be linearly stable for the strong ETG condition (blue), while the KBM could be close to marginality in the weak ETG condition (green). A discussion on the potential role of the ion-scale instability and turbulence is given in III. Importantly, the electron temperature gradient mode (ETG) is expected to be unstable in both conditions, motivating a detailed study of ETG-driven transport.

The rest of the article proceeds as follows: Sec. II describes the experimental evidence, gyrokinetic simulations, and a succinct review of the comparisons in Ref. 18 between the experimental values of electron thermal transport and measurements of density fluctuations vs the predicted ETG-driven transport and synthetic density fluctuation spectra. Section III discusses the role that the ion-scale instability and turbulence might play in the weak ETG condition. Section IV contains new projections for future high-k measurements in NSTX-U using nonlinear gyrokinetic simulation and a synthetic diagnostic for the new high-k scattering system. A brief summary and conclusions are stated in Sec. V.

II. MEASUREMENTS, MODELING, AND EXPERIMENT-MODEL COMPARISONS OF ETG FLUCTUATIONS AND TRANSPORT

In this section, we review the experimental measurements, nonlinear gyrokinetic simulations, and the experiment-model comparisons of ETG fluctuations and transport from NSTX NBI heated H-mode 141767 at $r/a \sim 0.7$, focusing on a strongly driven and a

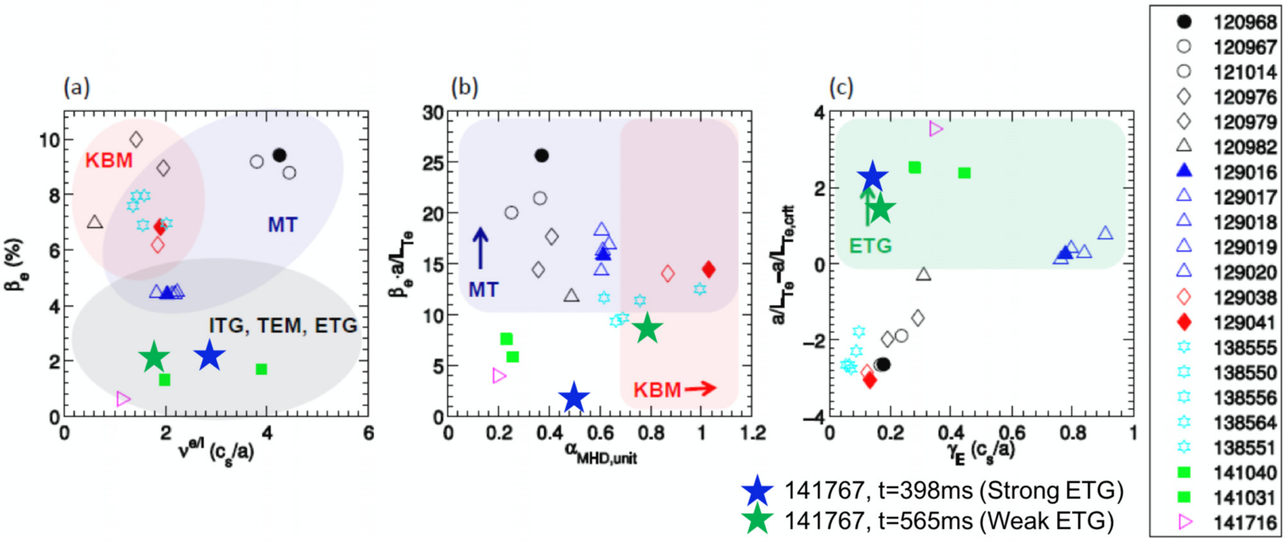

FIG. 1. Regime plots showing dominant instability from local GYRO linear simulations corresponding to various NSTX H-modes at $r/a \sim 0.6 - 0.7$, vs local parameters (courtesy of Guttenfelder[8]). (a) β_e vs $\nu^{e/i}$. (b) $\beta_e \cdot a/L_{\rm Te}$ vs $\alpha_{\rm MHD,unit}$. (c) $a/L_{\rm Te} - a/L_{\rm Te,crit}$ vs γ_E. Figure 1 from Ref. 11 has been updated with results from NSTX H-mode 141 767 studied in this article, indicated by the blue and green stars (conditions of strong and weak ETG turbulence drive, respectively). The definition of β_e uses the vacuum B_{T0} value at the magnetic axis while and $\alpha_{\rm MHD,unit}$ use the convention $B_{\rm unit}$ in the GYRO code.[10,24] Adapted with permission from Guttenfelder *et al.*, Nucl. Fusion **53**, 093022 (2013). Copyright 2013 IOP Publishing.

Published under license by AIP Publishing

weakly driven ETG turbulence condition. Additional details can be found in Refs. 17, 18, and 20.

A. Experimental evidence of ETG-driven transport

Direct experimental evidence of ETG-driven turbulence was provided via density fluctuation measurements from the 280 GHz high-k scattering system on NSTX.[21] The high-k scattering system had three operational channels at each time of interest, sensitive to turbulence wavenumbers in the range $(k_R, k_Z) \approx (11-19, 2.4-3.5)$ cm^{-1}, with normalized values $(k_R\rho_s^{\exp}, k_Z\rho_s^{\exp}) \approx (8-13, 1.5-2.5)$ for the strong ETG condition. For the weak ETG condition, $(k_R, k_Z) \approx (15-26, 1.5\text{–}3)$ cm^{-1}, or equivalently $(k_R\rho_s^{\exp}, k_Z\rho_s^{\exp}) \approx (10-18, 1-2)$. The quoted values for $\rho_s^{\exp} \approx 0.7$ cm use the TRANSP[22] local values of $T_e \sim 0.4$ keV and magnetic field $B_T \sim 0.4$ T. In what follows, we will use the normalization of the ion-sound gyro radius by B_{unit} to perform quantitative comparisons via synthetic diagnostic for high-k scattering, which we will note ρ_s (here $\rho_s \approx 0.2$ cm using $B_{\text{unit}} \approx 1.44$ T). In this work, we denote k_R the wavenumber component along the major radius R, and k_Z is the component in the vertical direction. The difference in notation with respect to Refs. 18 and 19 is clarified on Appendix A. These wavenumber components are computed independently for each measurement channel of the diagnostic via ray tracing calculations, following the propagation of a single ray modeling the microwave beam propagation in the plasma. The wavenumber resolution of the observed electron density fluctuations is $\Delta k \approx \pm 0.7$ cm^{-1} and a corresponding radial resolution $\Delta R \approx \pm 3$ cm. A view from the top of the ray-tracing solution for the probe and scattered beams is shown in Fig. 9(a).

With respect to transport, estimates of the electron thermal power are computed from power balance calculations in TRANSP.[22] A total electron thermal power of $P_e \approx 1.48 \pm 0.33$ MW was obtained for the strong ETG condition, and $P_e \approx 1.02 \pm 0.23$ MW for the weak ETG condition (the ± sign denotes the $1-\sigma$ error bar computed via error propagation analysis). As discussed in detail in Refs. 17 and 18, the reduction of ETG fluctuations at the weak ETG time was correlated with decreased electron thermal power levels. For reference, ion thermal power $P_i \sim 0.5-0.6$ MW for both conditions, lying within the uncertainty range of neoclassical levels predicted by NEO.[23]

The predictions taken from Fig. 1, along with the experimental electron-scale fluctuation measurements[17,18] and the anomalous electron thermal power levels from TRANSP, all motivate a detailed study of electron-scale turbulence and transport. In what follows, we will use gyrokinetic simulation to predict turbulent electron thermal transport levels and to model electron-scale density fluctuations measured via high-k scattering. The latter will be enabled via a synthetic diagnostic developed as part of this work.

B. Nonlinear gyrokinetic simulation

Local nonlinear gyrokinetic simulations were performed with the gyrokinetic code GYRO,[10,24] only accurately resolving electron-scale fluctuations characteristic of ETG turbulence $k_\perp\rho_s \gtrsim 1$. Owing to the neoclassical ion thermal transport levels, ion-scale turbulence existing at $k_\perp\rho_s \lesssim 1$ is assumed to play a negligible role. This is also consistent with linear and nonlinear ion-scale gyrokinetic simulations carried out in Ref. 18 for the present conditions. Some caveats to these assumptions are discussed in Sec. III.

Simulations were performed at the scattering location $r/a \sim 0.7$, resolving three gyrokinetic species (e^-, D, C), including electron collisions ($\nu_{ei} \sim 1$ a/c$_s$, but not ion collisions: cf. Sec. III B), background flow and flow shear ($M \sim 0.2, \gamma_E \sim 0.1-0.2$ a/c $_s, \gamma_p \sim 1$ a/c$_s$), and fully electromagnetic fluctuations $(\delta\phi, \delta A_{||}, \delta B_{||})$. Linear background profiles were simulated employing nonperiodic boundary conditions in the radial direction with typical buffer widths $\Delta_b \sim 2\text{–}3\rho_s$. An unusually large electron-scale simulation domain was employed $[(L_r, L_\theta) = (20, 20.6)\rho_s]$, translating to a wavenumber grid resolving minimum nonzero wavenumbers $dk_\theta\rho_s \approx 0.3$ and $dk_r\rho_s \approx 0.3$. Here k_θ and k_r are, respectively, the poloidal and radial wavenumbers of the turbulence that are internally defined in GYRO[10] and CGYRO.[25] The particular choices for the radial and poloidal wavenumber resolutions are $k_r\rho_s \epsilon [0.3, 40]$ and $k_\theta\rho_s \epsilon [0.3, 65\text{–}88]$, depending on the plasma condition [see Refs. 18 and 19 for additional details and discussion on the (k_r, k_θ) grid]. Parallel resolution employed 14 poloidal grid points (×2 signs of parallel velocity), 12 energies, and 12 pitch-angles (6 passing + 6 trapped). This choice of numerical grids was made according to previous convergence and accuracy tests for the GYRO code simulating micro-instabilities in the core NSTX[11] and was also tested for convergence in the present conditions.[18] The flux surface geometry is implemented by a Miller equilibrium.[26] The numerical resolution parameters result in simulations that consume ≈1 − 2 M CPU hours per simulation, carried out in the leadership supercomputer Edison at NERSC.

C. Experiment-model comparisons of ETG fluctuations and transport

In this subsection, we compare results from the nonlinear electron-scale gyrokinetic simulations to experimental values of electron thermal transport as well as to electron-scale turbulence measurements from high-k scattering using a synthetic diagnostic.[19] Using experimental profile values as input shows that electron-scale gyrokinetic simulation corresponding to the strong ETG condition can only provide ≈30% of the experimental electron thermal power estimate from TRANSP (recall $P_e^{\exp} \approx 1.48 \pm 0.33$ MW) and motivates a sensitivity study of the electron thermal power to the ETG turbulence drives. With respect to the weak ETG condition, the experimental electron thermal transport level can be matched within experimental uncertainty of the simulation drive inputs $a/L_{Te}, a/L_{ne}$ (normalized electron temperature and density gradients[18]).

We present sensitivity scans corresponding to the strong ETG condition for the main ETG turbulence drive mechanisms $(a/L_{Te}, a/L_{ne}, q, \hat{s})$. Here $a/L_{Te} \equiv -a\nabla T_e/T_e$ and $a/L_{ne} \equiv -a\nabla n_e/n_e$, q is the magnetic safety factor, and $\hat{s}$ is the magnetic shear (we note $a/L_{Te}, a/L_{ne}$ interchangeably by $\nabla T, \nabla n$ in the rest of this paper). The background electron temperature and density gradients are scanned within $+1-\sigma$ experimental uncertainty, while q is scaled by −10% and $\hat{s}$ is scanned by +20%, all in the direction of increasing the ETG drive (specific values are summarized on Table V in Appendix C). The uncertainties in $a/L_{Te}, a/L_{ne}$ were computed from uncertainties in the background electron density and temperature profiles followed by a Monte Carlo analysis approach, and the values of −10% q and +20% $\hat{s}$ were taken as reasonable estimates of the equilibrium reconstruction uncertainty.

A total of five simulations corresponding to the strong ETG condition are used to compare to experiment for the following observables: electron thermal power P_e (MW), the shape of the wavenumber spectrum $S(k_\perp)$, and the fluctuation level ratio between the strong and the weak ETG conditions $\langle S\rangle^{\mathrm{strongETG}}/\langle S\rangle^{\mathrm{weakETG}}$. As shown in Refs. 18 and 19, these result in powerful metrics that allow a quantitative assessment of the fidelity of each simulation in the comparison to the experimental quantities. The rationale behind this work is to find simulation conditions for the strong ETG case where local nonlinear gyrokinetic simulation can simultaneously explain all the mentioned observables.

1. Electron thermal transport

Figure 2(a) summarizes the electron thermal power comparisons. The experimental level lies in the gray horizontal band at $P_e^{\mathrm{exp}} \approx 1.48 \pm 0.33$ MW, computed via TRANSP. The uncertainties in P_e are computed via error propagation of the electron power balance equation implemented in TRANSP. The base simulation uses the experimental input profile parameters in the GYRO inputs and shows clear under-prediction of the experimental power level. Scaling $(+a/L_{Te}, -a/L_{ne})$ by $1-\sigma$ (noted as $(\nabla T, \nabla n)$ in black) increases the predicted P_e with respect to the base case, but still under-predicts the experimental P_e. However, scaling q and $\hat{s}$ in addition to a combination of a/L_{Te} or a/L_{ne} in the GYRO inputs is shown to reproduce the experimental electron thermal power levels, as shown by the purple and light green bars. Scanning all four parameters $(a/L_{Te}, a/L_{ne}, q, \hat{s})$ is shown to drive ETG too strongly (noted $(\nabla T, \nabla n, q, \hat{s})$ in the dark green), leading to an over-prediction of the experimental P_e.

Figure 2(a) shows that local, nonlinear, electron-scale gyrokinetic simulation is able to both under- and over-predict the experimental electron thermal transport levels P_e (MW) within a sensitivity scan of the most pertinent ETG drive terms. Additionally, Fig. 2(a) shows that simultaneously scanning a/L_{Te} and a/L_{ne} by $1-\sigma$ was not sufficient to match P_e, but modifying q and $\hat{s}$ was necessary to reproduce the experimental thermal power levels. This highlights the significant impact of q and $\hat{s}$ in the present conditions, which will be further highlighted Sec. II C 2–II C 4.

2. Fluctuation level ratio

Owing to the absence of absolute calibration in the high-k scattering power level, an assessment of the measured fluctuation power compared with simulated fluctuation power is not possible. Here we choose to quantify the fluctuation level ratio between the strong and weak ETG conditions. The metric $\log_{10}[\langle S\rangle^{\mathrm{strong\,ETG}}/\langle S\rangle^{\mathrm{weak\,ETG}}]$ is chosen, where $\langle . \rangle$ denotes the arithmetic average power between channels 1–3. The use of the $\log_{10}$ is motivated by the fact that the quantity $\langle S\rangle^{\mathrm{strong\,ETG}}/\langle S\rangle^{\mathrm{weak\,ETG}}$ can vary by $2-3$ orders of magnitude in the sensitivity scans performed. In the comparisons shown, only the quantity $\langle S\rangle^{\mathrm{strong\,ETG}}$ is varied, while $\langle S\rangle^{\mathrm{weak\,ETG}}$ is kept constant, and calculated from a simulation for the weak ETG condition which matched the electron thermal power P_e (scaling a/L_{Te} and a/L_{ne} by $1-\sigma$ uncertainty, not shown here).

Figure 2(b) shows the result of the fluctuation level ratio comparisons between the five simulations for the strong ETG condition and the experimental range in gray. The experimental level is shown by the gray horizontal band, where the uncertainty is calculated from uncertainties in the fluctuation levels by channels 1–3 of the high-k scattering system. The base simulation is shown to clearly under-predict the experimental fluctuation level ratio, shown by the magenta bar. This means that the strong ETG simulation with the base nominal experimental parameters (magenta) is too weakly driven to reproduce the ratio of fluctuation levels, which is also consistent with Fig. 2(a). Simulations scanning $(a/L_{ne}, q, \hat{s})$-light green and $(a/L_{Te}, a/L_{ne},$

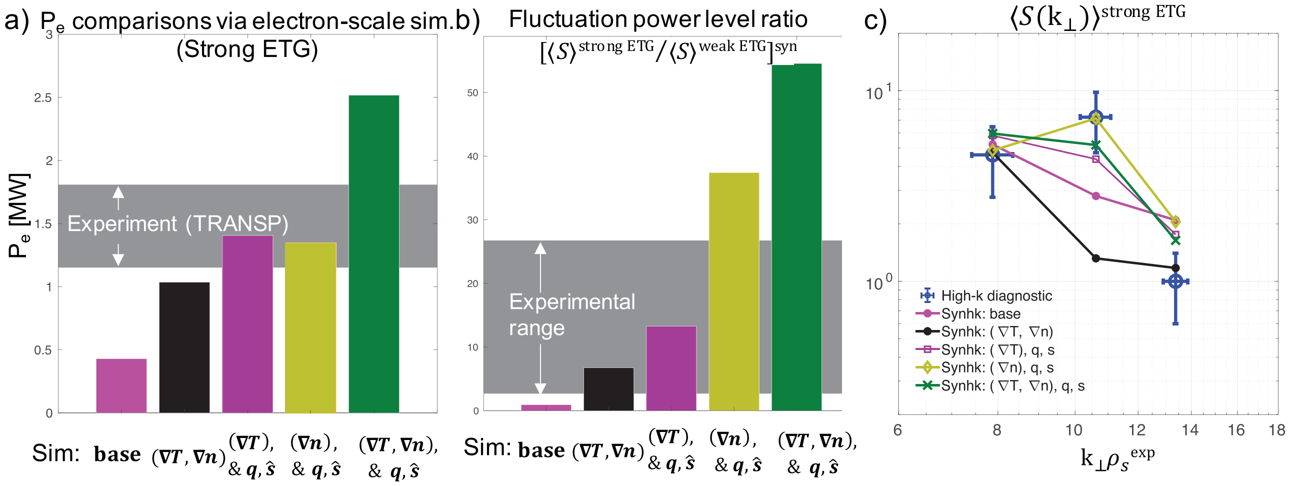

FIG. 2. (a) Comparisons between experimental (TRANSP) and simulated electron thermal power from local electron-scale simulation corresponding to the strong ETG condition. Scans in the equilibrium inputs ∇T_e, ∇n_e are made within experimental uncertainty, safety factor q is varied by 10% and magnetic shear $\hat{s}$ by 20%. (b) Comparisons between experiment and simulation of the fluctuation level ratio between the strong and weak ETG conditions, quantified by the metric $\log_{10}[\langle S\rangle^{\mathrm{strongETG}}/\langle S\rangle^{\mathrm{weakETG}}]$, where $\langle . \rangle$ denotes the average power between channels 1–3. (c) Comparisons between the measured high-k density fluctuation wavenumber spectrum and simulated wavenumber spectrum by local electron-scale GYRO simulation corresponding to the strong ETG condition. Adapted with permission from Ruiz *et al.*, Plasma Phys. Controlled Fusion **61**, 115015 (2019). Copyright 2019 IOP Publishing.

Published under license by AIP Publishing

$q,\hat{s}$)-dark green exhibit an over-prediction in the fluctuation level ratio with respect to the levels measured by experiment, suggesting that for these parameter scans, ETG was too strongly driven in the strong ETG condition. However, simulations scanning $(a/L_{Te}, a/L_{ne})$-black and $(a/L_{Te}, q, \hat{s})$-purple both lie within the experimental range. As in Fig. 2(a), Fig. 2(b) shows how the fluctuation level ratio between the strong and weak ETG conditions can be both under- and over-predicted by gyrokinetic simulation when sensitivity scans in the main ETG drive mechanisms are performed. This shows that local nonlinear electron-scale gyrokinetic simulation can explain the fluctuation level ratio between the strong and weak ETG conditions.

3. Wavenumber spectra shape

Comparisons of the shape of the wavenumber spectrum are shown in Fig. 2(c), corresponding to the same five gyrokinetic simulation scans for the strong ETG condition. The experimental wavenumber spectrum is depicted by blue circles and is scaled in amplitude in order to yield comparisons of the *shape* of the wavenumber spectrum.

Figure 2(c) shows that neither the base simulation (magenta) nor the simulation scaling $(a/L_{Te}, a/L_{ne})$ (black) is able to reproduce the shape of the experimental wavenumber spectrum, computed from the three high-k scattering channels. Figure 2(c) also qualitatively shows that the best agreement in the shape of the wavenumber spectrum is shown for simulations which scaled q and $\hat{s}$ in the inputs, in addition to combinations of a/L_{Te} and a/L_{ne}, as shown in purple, light green, and dark green. This highlights once more the significant sensitivity that q and $\hat{s}$ have on the present ETG conditions, now showing how q and $\hat{s}$ can modify the shape of the ETG spectrum. Particularly, the best agreement is shown for the simulation run with scaled $(a/L_{ne}, q, \hat{s})$, depicted in light green. This shows that electron-scale simulation can also explain the *shape* of the measured density fluctuation wavenumber power spectrum.

4. Experiment-model comparison of the frequency and wavenumber spectrum

As detailed in Ref. 18, the fidelity of the previous comparisons can be quantitatively assessed via the use of validation metrics. These showed that simulations scanning $(a/L_{Te}, q, \hat{s})$ and $(a/L_{ne}, q, \hat{s})$ exhibit the best quantitative agreement. Remarkably, both simulations were shown to reproduce the experimental level of the electron thermal power [Fig. 2(a)]. Simulation scanning $(a/L_{ne}, q, \hat{s})$ will be used in Sec. IV to make projections of frequency and wavenumber spectra with the new high-k system to be installed in NSTX-U.[27]

In Fig. 3 are shown the frequency and wavenumber spectra comparisons for the simulation scanning $(a/L_{ne}, q, \hat{s})$. Although the frequency spectrum was strongly influenced by Doppler shift,[18,19] a successful validation work should still match the measured frequency spectrum as a consistency check of the simulated turbulence fluctuations and the synthetic diagnostic. Figure 3(a) shows that the synthetic frequency spectrum agrees well with the measured spectrum. As expected, the $f=0$ peak and the background noise level are different between experiment and simulation (due to stray radiation and possibly electronic noise setting the experimental background), but only the broadband fluctuations at $f\sim -1$ MHz should be visually compared. For reference, all five simulations presented here exhibited reasonably good agreement in the peak and the width of the frequency spectrum. As shown in Fig. 3(b), the agreement in the wavenumber spectrum is also satisfactory.

III. DISCUSSION OF THE ION-SCALE INSTABILITY AND TURBULENCE

Following successful validation of the electron-scale gyrokinetic simulations for the strong ETG condition in Sec. II, in this section we discuss the potential role that the ion-scale instability and turbulence might play in the weak ETG condition. Linear gyrokinetic simulations in subsection III A suggest that the ion-scale instability is expected to

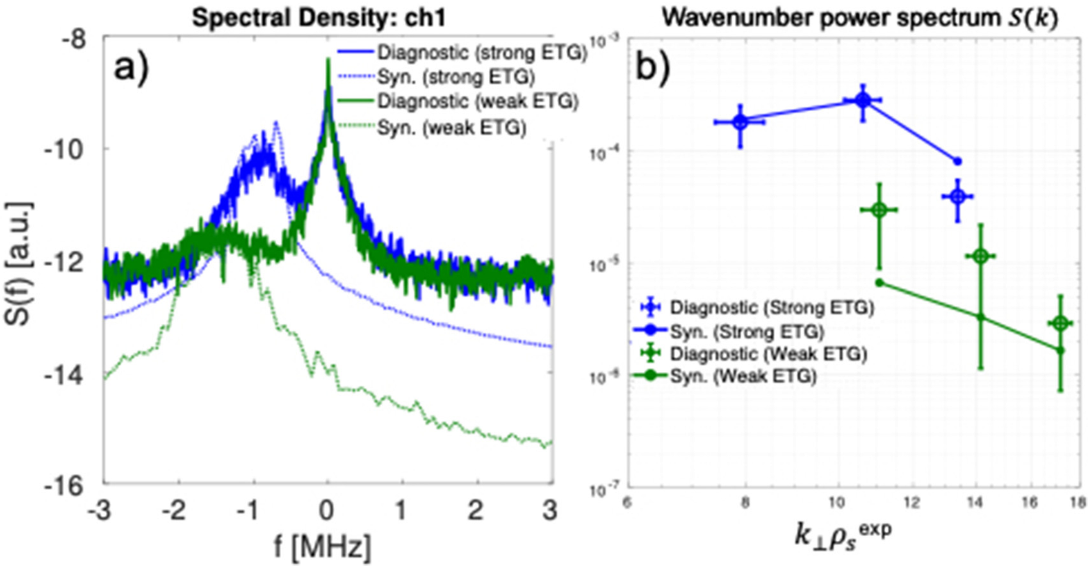

FIG. 3. (a) Frequency spectra and (b) wavenumber spectra comparisons between experiment and simulation, corresponding to the best matched GYRO simulation for the strong ETG condition [simulation scanning $(a/L_{ne}, q, \hat{s})$ in the inputs], as quantified by the validation metrics in Ref. 18. Frequency spectra corresponds to channel 1, where channels 2 and 3 exhibit similar agreement. Reproduced with permission from Ruiz *et al.*, Plasma Phys. Controlled Fusion **61**, 115015 (2019). Copyright 2019 IOP Publishing.

play a negligible role in the strong ETG condition, while the experimental profiles are shown to sit close to the critical KBM threshold in the weak ETG condition. Subsection III B shows how ion–ion collisions can strongly affect the ion-scale turbulent fluctuation levels via zonal flow damping in these near-marginal ion-scale turbulent conditions for the weak ETG case.

A. Effect of beta on ion-scale instability

The linear effect of electron beta β_e on the ion-scale instability is shown to be different between the strong and weak ETG conditions. This might be specifically significant for the weak ETG condition since the experimental value of β_e is shown to be very close to the instability threshold of the KBM instability.

Figures 4(a) and 4(b) show the real frequency ω_r and linear growth rate γ from scans in the electron beta β_e carried out for a particularly unstable ion-scale wavenumber ($k_\theta\rho_s = 0.48$) for the strong ETG condition. At low β_e, an ion-directed, ballooning parity instability is shown to be the fastest growing mode, possibly identified to a trapped electron mode or ubiquitous mode (noted TEM). The linear growth rate in (b) is shown to be weaker than the background $E \times B$ shearing rate. At increasing value of β_e, the linear growth rate is shown to decrease with β_e up to values of $\beta_e \approx 0.25\%$, in which the dominant instability is shown to transition to an electron-directed, tearing parity micro-tearing mode (MT). The experimental β_e value is shown to sit right at the critical beta for the transition between the TEM and MT mode. For beta values $>0.25\%$, the linear growth rate exhibits a weak, destabilizing dependence with β_e, characteristic of the MT mode. However, the MT linear growth rate is very close to the background $E \times B$ shearing rate. For even greater β_e values, the MT mode becomes subdominant to an ion-directed kinetic ballooning mode, exhibiting high growth rate values that clearly surpass the $E \times B$ shearing rate value. This β_e scan clearly shows three different instabilities can coexist for experimentally relevant NSTX plasma parameters. However, we point out that the TEM and MT modes are the most experimentally relevant for the present case, which are predicted to be suppressed by strong $E \times B$ shear in this condition and consistent with negligible transport produced by nonlinear ion-scale gyrokinetic simulation (not shown here). Note β_e here uses the B_{unit} convention in GYRO, and the uncertainty of β_e is on the order of 10%. The beta scans presented also preserved the value of beta-prime β' fixed. The $\alpha_{\text{MHD,unit}}$ value is shown to be $\approx$0.5 in this condition, suggesting the KBM may not be experimentally relevant in this condition as suggested by Fig. 1 and previous work.[11]

The black curve in Fig. 4 shows linear scans computed including the full electromagnetic field perturbations $(\delta\phi, \delta A_{||}, \delta B_{||})$. The blue linear scans only included $(\delta\phi, \delta A_{||})$ perturbations. The TEM and MT modes are shown to be unaffected by the inclusion of $\delta B_{||}$ perturbations; however, the KBM is shown to be stabilized without $\delta B_{||}$ perturbations.

Figure 5 shows the corresponding β_e scans for the weak ETG condition. In this case, an electron-directed, ballooning parity TEM mode is most unstable at low beta. The growth rate is shown to be higher than the background $E \times B$ shearing rate. When full perturbations of the electromagnetic field are included (black line), the TEM mode transitions to an ion-directed, ballooning parity KBM mode at $\beta_e \approx 0.35\%$, with linear growth rates greatly exceeding the background $E \times B$ shearing rate. The transition from TEM to KBM happens within 20% of the experimental β_e value. This suggests the KBM might have an important role to play in the weak ETG condition. If only $(\delta\phi, \delta A_{||})$ perturbations are included in the simulation, the KBM is stabilized and the TEM transitions to an electron-directed, tearing parity MT mode that ultimately transitions to the KBM for $\beta_e \approx 0.9\%$ (greatly exceeding the experimental β_e). It is worth pointing out how

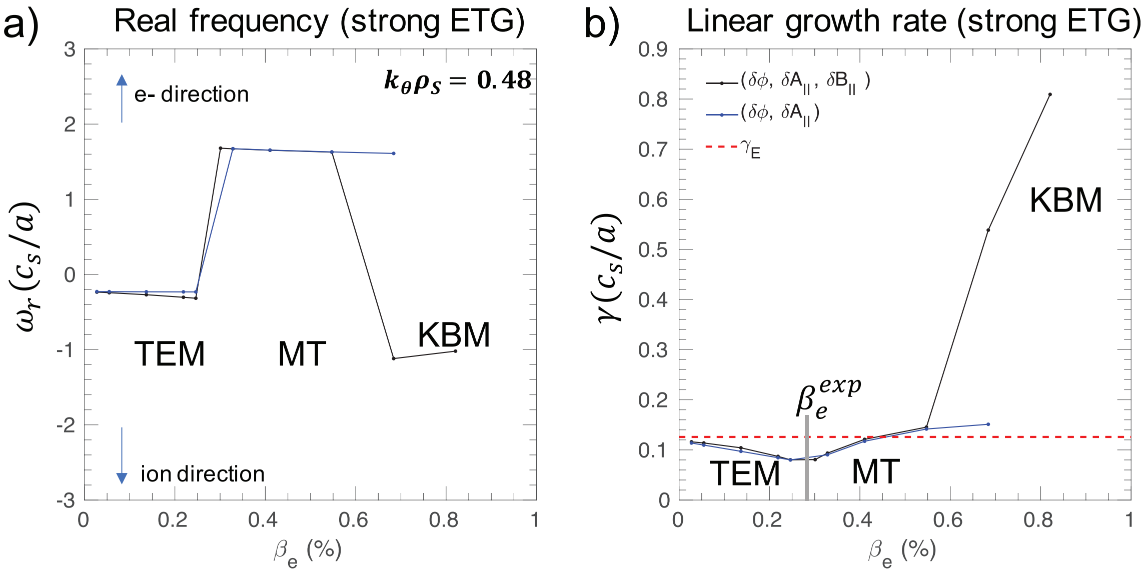

FIG. 4. (a) Real frequency from a linear beta scan for $k_\theta\rho_s = 0.48$ for the strong ETG condition. (b) Corresponding linear growth rate from a linear beta scan for $k_\theta\rho_s = 0.48$.

Published under license by AIP Publishing

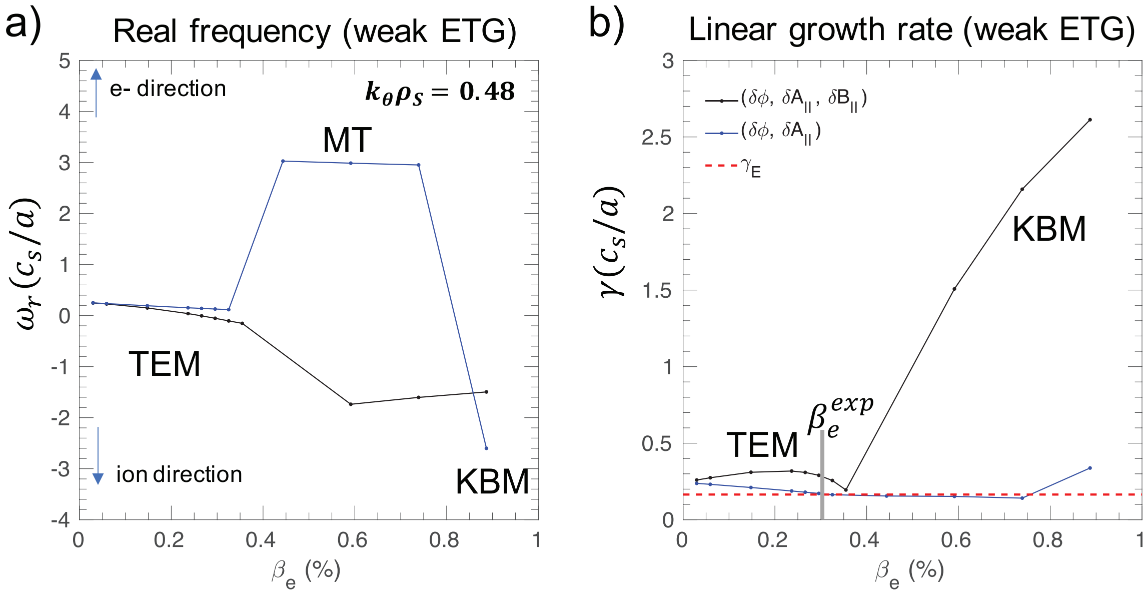

FIG. 5. (a) Real frequency from a linear beta scan for $k_\theta \rho_s = 0.48$ for the weak ETG condition. (b) Corresponding linear growth rate from a linear beta scan for $k_\theta \rho_s = 0.48$.

the TEM at low beta is shown to be stabilized when $\delta B_{||}$ perturbations were not included in the simulation. The uncertainty value of β_e is about 10%, showing the transition to KBM is outside uncertainty. However the $\alpha_{\mathrm{MHD,unit}}$ value is shown to be ≈0.7–0.8 in this condition, suggesting KBM may be experimentally relevant as suggested by Fig. 1 and by previous work.[11,28] It may also be that additional effects such as the inclusion of a fast-ion species could lower the KBM limit within the uncertainty range of the experimental beta value. Additional analysis should be performed to address this speculation.

Although very preliminary, these linear beta scans for ion-scale modes have shown how the KBM might be experimentally relevant in the weak ETG condition, but not at the strong ETG condition, which as shown in this article is dominated by ETG.

B. Effect of ion–ion collisions on ion-scale turbulence

All the available experimental evidence shown in this article has pointed to ETG-driven turbulence as the main contributor to electron thermal transport both in the strong and weak ETG conditions. However, the state and the role that ion-scale turbulence might play in the weak ETG condition is still not fully understood and requires more careful analysis which we partly present here.

We collect the available evidence for the weak ETG condition: (1) the measured high-k fluctuation power is lower than for the strong ETG condition; (2) the ion-scale linear growth rate can exceed the background $E \times B$ shearing rate, and lies close to the linear β_e threshold for the KBM; (3) ion thermal transport is very close to the neoclassical levels predicted by NEO;[23] (4) nonlinear electron-scale gyrokinetic simulation can reproduce the electron thermal power within uncertainty in ∇T and ∇n;[18] and (5) ion-scale nonlinear simulation showed that the background $E \times B$ shear can suppresses ion-scale turbulence.[18] Although the ion-scale instability might be linearly unstable, nonlinear simulation shows that ion-scale turbulence is suppressed, suggesting a negligible role for the weak ETG condition. In this section, we show ion-scale turbulence is nonlinearly suppressed by large zonal flow amplitudes, in a state reminiscent of a Dimits' shift regime,[29] and possibly linked to the recently observed subcritical fluctuations.[30] However, a strong TEM/KBM branch is destabilized within experimental uncertainty, yielding unphysical electron thermal power levels up to 10 times the experimental value.

Nonlinear ion-scale gyrokinetic simulations carried out for the weak ETG condition show the important effect of ion–ion collisions on zonal flow. For two decades, it has been known that ion–ion collisions can act as a damping mechanism on the zonal flow.[31–33] These were not modeled in the simulations presented in Sec. II. Ion–ion collisions are expected to be negligible for finite turbulence amplitudes dominated by turbulence interactions with the zonal flow. In situations of fully developed turbulence commonly encountered in the tokamak core, ion–ion collisions tend to play a negligible role in damping the zonal flow. However, ion–ion collisions can become important in conditions where the turbulence is very close to the nonlinear threshold. This effect can be enhanced at high collisionality values $\nu_{ei} \sim 1$ c_s/a in the present conditions. These are precisely the conditions found for the weak ETG case and motivate this preliminary analysis on the effect of ion–ion collisions on ion-scale turbulence.

The ion-scale simulations model radial and poloidal wavenumbers necessary to resolve ion-scale turbulence, here $k_r \rho_s \,\epsilon\, [0.08, 4]$ and $k_\theta \rho_s \,\epsilon\, [0.08, 1.1]$. We model drift-kinetic electrons, gyrokinetic main deuterium ions, and a gyrokinetic carbon impurity. Simulations were performed at the local scattering location $r/a \sim 0.7$, including electron-ion collisions $\nu_{ei} = 4\pi n_e e^4 \log \Lambda / (2T_e)^{3/2} m_e^{1/2} \approx 1$ c_s/a (via a pitch-angle scattering Lorentz operator), ion–ion collisions $\nu_{ii} = \nu_{ei} \sqrt{\frac{m_e}{m_i}} (\frac{T_e}{T_i})^{3/2} \frac{n_i}{n_e} Z_i^2$, fully electromagnetic fluctuations $(\delta\phi, \delta A_{||}, \delta B_{||})$, background toroidal flow, and flow shear ($M \sim 0.2$, perpendicular flow shear $\gamma_E \sim 0.1 - 0.2$ and parallel flow shear $\gamma_p \sim 1$). Linear

Published under license by AIP Publishing

background profiles were simulated, employing nonperiodic boundary conditions in the radial direction, implemented in GYRO via buffer damping regions of radial width $\Delta_b \sim 8\rho_s$. Parallel resolution employed 14 poloidal grid points ($\times 2$ signs of parallel velocity), 12 energies, and 12 pitch-angles (6 passing + 6 trapped). This choice of numerical grids was made according to previous convergence and accuracy tests for the GYRO code, simulating micro-instabilities in the core of NSTX,[11] and was also tested for convergence for the present conditions.[18]

Figure 6 shows the total, saturated values of the electron and ion thermal power P_e, P_i (MW) computed via ion-scale gyrokinetic simulation for different values of the driving parameter a/L_{Te}. All simulations were run using a constant, scaled value of a/L_{ne} of $1-\sigma$ uncertainty. In red are shown simulations run without the inclusion of ion–ion collisions. Looking at the red curve, ion-scale simulation predicts negligible P_e and P_i for $a/L_{Te} < 5$ values, but a highly unstable TEM/KBM branch for $a/L_{Te} > 5$. The letters A–C denote simulations run with input values of $a/L_{Te} = 4.5, 4.8, 5.4$, respectively. The magenta curves are the result of three simulations that were restarted from A–C by including ion–ion collisions on the zonal flow $n = 0$. The saturated values of P_e and P_i from such simulations are shown by the letters D–F. Figure 6 shows that ion–ion collisions can have a substantial effect on the turbulence saturated state for A and B, leading to the highly unstable turbulence regimes D and E. However, C and F predict essentially the same turbulence state and transport. These results suggest that ion–ion collisions are mostly important in close to threshold conditions (close to marginality as in A and B), but not far from threshold (as in C).

The role of ion–ion collisions on A–C are more clearly shown in Figs. 7(a)–7(c). These show time traces of the electromagnetic field fluctuation amplitudes $(\delta\phi, \delta A_{||}, \delta B_{||})$ for the turbulence $(\sum n > 0)$ and zonal flow $(n = 0)$, corresponding to simulations A–F in Fig. 6. Simulations in Fig. 7 are run with the same value of electron density gradient (scaled by $1-\sigma$) but different electron temperature gradients as input. All three simulations in Fig. 7 are divided in three time phases. In the first time phase, simulations are started with a zero value of $E \times B$ shearing rate γ_E and zero value of ion–ion collision frequency $\nu_{ii,ZF} = 0$. In this phase, turbulence fluctuations follow the linear exponential growth phase for the first 50–100 a/c$_s$. After the linear growth phase, fluctuations saturate at high amplitudes without the suppressing effect of γ_E. In the second phase of the simulations, the experimental value of $E \times B$ shear is included and corresponds to phases A–C, respectively, in Figs. 7(a)–7(c). In this phase, the finite n turbulence fluctuations are suppressed by the effect of γ_E. In Figs. 7(a) and 7(b), the state is dominated by strong potential fluctuations of the zonal flow (indicated by $\phi_{n=0}$, black dashed line) and the turbulence is shown to be fully suppressed. Negligible transport is predicted in this time phase, as can also be seen from A and B in Fig. 6. In Fig. 7(c), the state is dominated by strong finite-n, turbulence fluctuations, producing high values of transport (corresponding to C in Fig. 6). The unrealistic transport values greatly exceed the experimental transport levels $\sim$ tenfold.

In the third phase of the simulations, the experimental value of the ion–ion collision frequency is included, preserving the previous parameters constant (γ_E, etc.). They are phases D–F, respectively. In Figs. 7(a) and 7(b), the large value of the zonal flow amplitude is shown to be strongly damped by the inclusion of finite ν_{ii}. This has the effect of destabilizing finite-n perturbations since now the weaker zonal flows are not able to efficiently regulate the turbulence. In D and E, finite-n perturbations are shown to saturate at very high amplitudes.

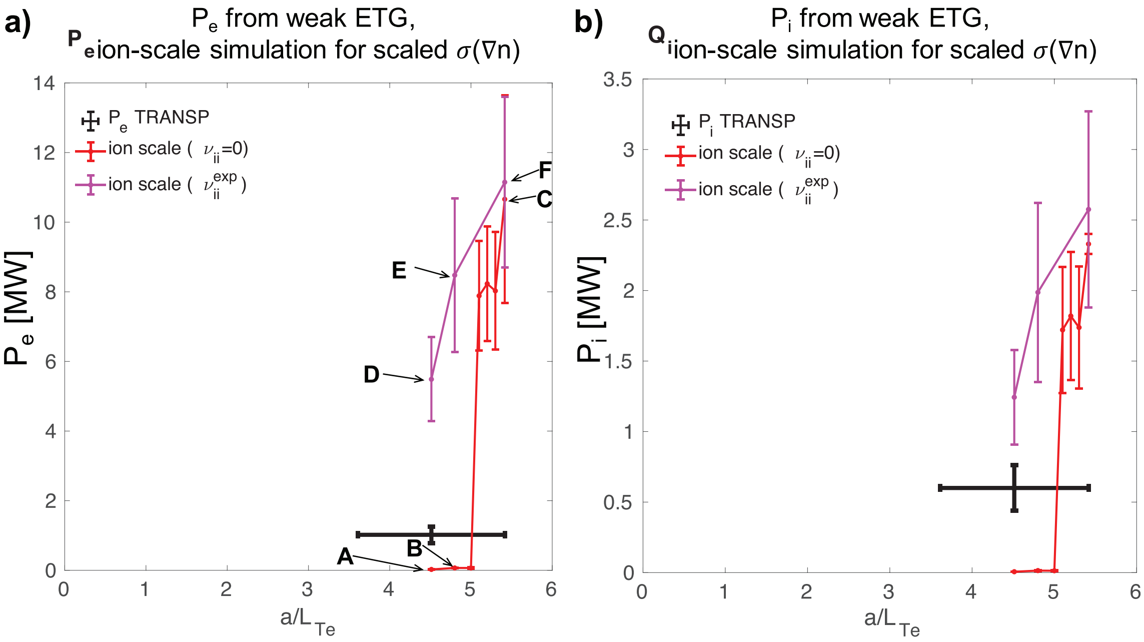

FIG. 6. (a) Electron thermal power from ion-scale simulation run with scaled density gradient value within 1σ uncertainty, for different values of electron temperature gradient a/L_{Te}. In red is shown simulation output when the value of ion–ion collision frequency ν_{ii} was set to 0. In magenta is shown simulation output when the value of ion–ion collision frequency was set to the experimental value $\nu_{ii} = \nu_{ii}^{exp}$ was set to 0. (b) Same as (a) but showing the ion thermal power P_i instead of the electron thermal power P_e.

Published under license by AIP Publishing

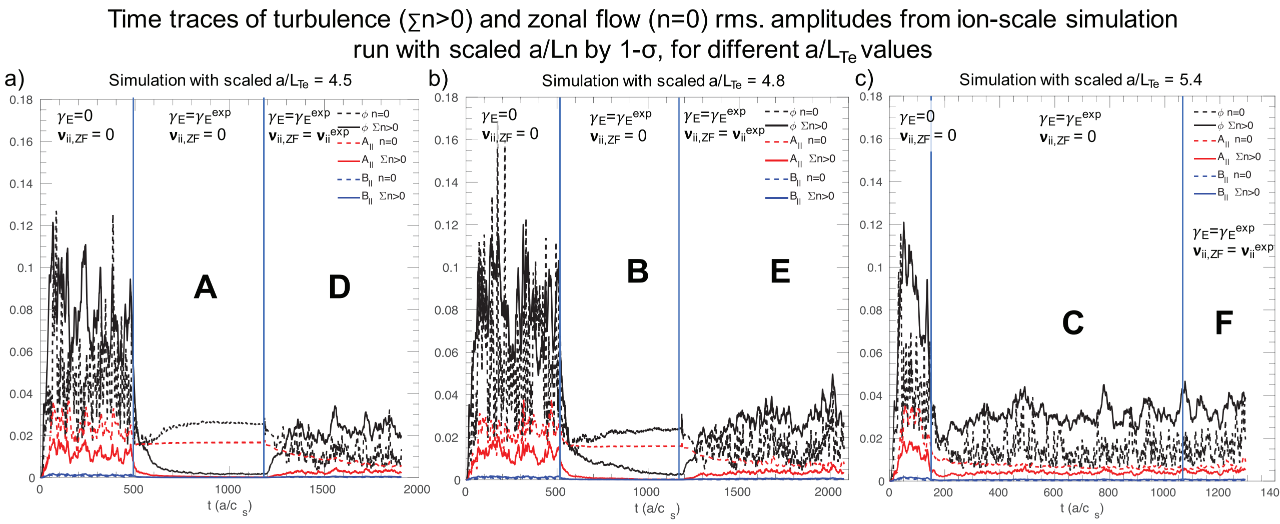

FIG. 7. Time traces of the electromagnetic field root mean square fluctuation amplitudes $(\phi, A_{||}, B_{||})$ for the turbulence $(\sum n > 0)$ and zonal flow $(n = 0)$, corresponding to simulations A–F in Fig. 6. All simulations were run with a scaled value of a/L_{ne} within $1-\sigma$ uncertainty. (a) Simulation was run using $a/L_{Te} = 4.5$. (b) Simulation was run using $a/L_{Te} = 4.8$. (c) Simulation was using $a/L_{Te} = 5.4$.

As can be seen from Figure 6, phases D and E produce some 6–8 MW of electron thermal power, clearly over-predicting the experimental value of $P_e^{exp} \sim 1$ MW. In Fig. 7(c), turbulence was already shown to be strongly driven in phase C, and the inclusion of ion–ion collisions in F is shown to have a negligible effect on the dynamics of the zonal flow, barely affecting the saturated levels and transport. In summary, Figs. 6 and 7 suggest that ion–ion collisions can have a very important effect on the ion-scale turbulence amplitude via the damping of zonal flows in close to marginal conditions and at high values of collisionality $\nu_{ei} \sim 1$ c$_s$/a. However, the effect is shown to be negligible in far from threshold conditions, exhibiting finite amplitude turbulence fluctuations.

Figures 8(a) and 8(b) show the time traces of electromagnetic field fluctuation amplitudes $(\delta\phi, \delta A_{||}, \delta B_{||})$, similar to Fig. 7, but this

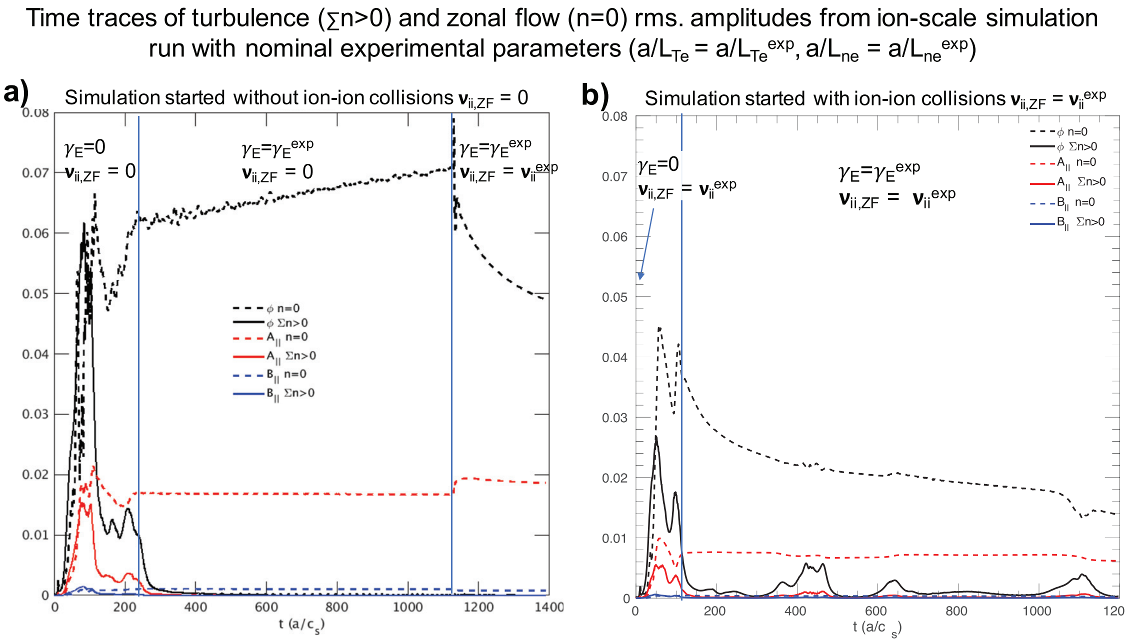

FIG. 8. Time traces of electromagnetic field root mean square fluctuation amplitudes $(\phi, A_{||}, B_{||})$, similar to Fig. 7, but this time carried out for the nominal, experimental profile values (in particular, experimental a/L_{ne} and a/L_{Te}). (a) The simulation is started at $t = 0$ a/c$_s$ using ion–ion collision frequency set to 0 $(\nu_{ii,ZF} = 0)$. (b) The simulation is started at $t = 0$ a/c$_s$ using ion–ion collision frequency set to the experimental value $(\nu_{ii,ZF} = \nu_{ii}^{exp})$.

Published under license by AIP Publishing

time corresponding to simulations carried out for the nominal, experimental profile values (in particular, experimental a/L_{ne} and a/L_{Te}). As in Fig. 7, simulations are started with a zero value of $E \times B$ shearing rate ($\gamma_E = 0$). In Fig. 8(a), the ion–ion collision frequency is initially set to 0 ($\nu_{ii,ZF} = 0$); in Fig. 8(b), the ion–ion collision frequency is set to the experimental value ($\nu_{ii,ZF} = \nu_{ii}^{\text{exp}}$). In the second phase, the experimental value of γ_E is included, which shows to suppress the finite-n modes. However, in the absence of ion–ion collisions in Fig. 8(a), the zonal flows are not saturated and exhibit n = 0 potential perturbations that have a linear dependence in time ($|\delta\phi_{n=0}|^2 \propto t$). This behavior is not observed in the presence of ion–ion collisions in Fig. 8(b) (after t $\gtrsim$ 120 a/c$_s$). This suggests the undamped zonal flow amplitudes in Fig. 8(a) are linked to the absence of ion–ion collisional damping on the zonal flows. In Fig. 8(b), one can observe sudden bursts of finite-n perturbations at $t \approx 450, 650, 1100$ a/c$_s$ (bold black line). These are in fact lone, large-scale eddies, occupying most of the simulation domain and producing non-negligible levels of instantaneous transport; however, they are eventually damped by the strong zonal flows present, producing negligible time-averaged transport levels. The observation of lone, large-scale eddies, occupying most of the simulation domain, is reminiscent of the subcritical transition to ITG turbulence observed in MAST gyrokinetic simulations.[30]

The behavior of undamped, linear dependence of the zonal flow in time observed in Fig. 8(a) is consistent with seminal work by Rosenbluth and Hinton.[31,32] When subject to a random and statistically stationary noise source,[31,32] showed that the zonal mean square potential can increase linearly in time. This behavior appears to be qualitatively similar to that observed in the outer core of this NSTX H-mode, in which the strongly suppressed finite-n fluctuations could act as the random and statistically stationary noise source in Refs. 31 and 32 (this might not be the case in the case of finite fluctuation amplitudes). One last time phase is shown in Fig. 8(a) by including ion–ion collisions (after $t \approx 1130$ a/c$_s$). In this regime, the main effect of finite ν_{ii} is on the zonal flow amplitude, exhibiting a nearly exponential decay. This behavior was also observed in Refs. 31 and 32. Unfortunately, the simulation in Fig. 8(a) was not run for long enough in order to observe the final saturated state of the zonal flow due to the large computational time needed for completion.

These ion-scale gyrokinetic simulations have shown that ion–ion collisions can have an important effect in damping zonal flows in close to threshold conditions, but not in far from threshold conditions. Strong zonal flows are shown to develop in the absence of ion–ion collisional damping on the zonal flow, and ion-scale turbulence fluctuations are strongly suppressed. When ion–ion collisions are included, zonal flows are strongly damped and ion-scale turbulence grows to unphysically large amplitudes. This suggests zonal flows, in addition to background $E \times B$ shear, can strongly suppress ion-scale turbulence in the weak ETG condition. Additionally, we have shown that a TEM/KBM branch can become unstable and lead to unphysically large ion and electron thermal powers. Previous work performed for an NSTX H-mode[11,28] has in fact highlighted that a hybrid TEM/KBM mode can produce experimentally relevant P_e. Further analysis would need to be performed to shed further light on this issue.

There are important caveats worth pointing out in the analysis of this subsection. We have used the "simple" Lorentz collision operator, which only models pitch-angle scattering collisions and no energy-diffusion. The high collisionality of these plasmas ($\nu_{ei} \approx 1$ c$_s/a$) suggests the Lorentz model might not be valid in these regimes, and advanced collisional models such as implemented in CGYRO[25] might be needed. In fact, recent work using the CGYRO code has shown that the residual zonal flow potential calculated using the advanced Sugama collision operator can vary by close to an order of magnitude at high levels of electron collisionality (similar to those used here) with respect to the simpler Lorentz model implemented in GYRO. This work was carried out simulating ITG turbulence for the GA standard case.[34] The results presented in this subsection motivate further work to understand the role of ion–ion collisions on the zonal flow, and the possible implications for the turbulence saturated levels and for cross-scale coupling interactions in realistic plasma conditions for the spherical tokamak.

As a clarifying note, ion–ion collisions were shown to play a negligible role in the electron-scale simulations from Sec. II.

IV. PROJECTIONS FOR HIGH-*k* MEASUREMENTS IN NSTX-U

Having successfully validated electron-scale gyrokinetic simulations in the current NSTX discharge, in this section we make use of the predicted turbulence fluctuations via gyrokinetic simulation to make preliminary projections for the new high-k scattering system that is currently under development for NSTX-U.[27] The new high-k scattering system will employ a 693 GHz microwave beam that will replace the 280 GHz beam in NSTX. The new scattering geometry and smaller beam wavelength is projected to enable measurements of up to $k_\perp > 40$ cm^{-1} in a spatial range from $r/a = 0.1$ out to $r/a = 0.99$. A detailed description of the Gaussian probe beam, launch optics, scattering and receiver optics, receiver hardware, and electronics is presented in Ref. 27.

The projections that follow represent a reduced subset of potential high-k measurements in NSTX-U. We restrict ourselves to $r/a \approx 0.7$ in the hypothetical scenario of NSTX discharge 141767 which was the object of the validation work presented in Sec. II. Although limited in scope, the projections show the enhanced capability for measuring the most relevant parts of the high-k density fluctuation wavenumber spectrum (so-called streamers[5,6]), which were not possible using the high-k system in NSTX.

A. Scattering geometry, *k*-selection, and *k*-resolution

The new high-k scattering geometry was designed to enable measurements of higher k_θ and smaller k_r wavenumber components of the turbulence than those accessed by the NSTX high-k system. Figure 9(a) shows a view from the top of the NSTX high-k scattering system, where the trajectories of the probe and scattered beams from 141767 are computed via ray-tracing. The near-tangential scattering geometry is suited for high k_r and smaller k_θ components. The scattering geometry for the NSTX-U high-k system is shown in Figs. 9(b) and 9(c). The probe beam in the new high-k scattering system propagates near the midplane but more perpendicularly to the magnetic field than the NSTX system, allowing lower k_r and higher k_θ measurements.

The new high-k scattering system is also designed with the capability for upward and downward scattering. Here we present projections for upward scattering in which the probe beam is launched directed slightly downwards from the midplane, while the scattered beams are directed upwards in most conditions [Fig. 9(c)]. This geometry will allow us to sample the most relevant parts of the high-k

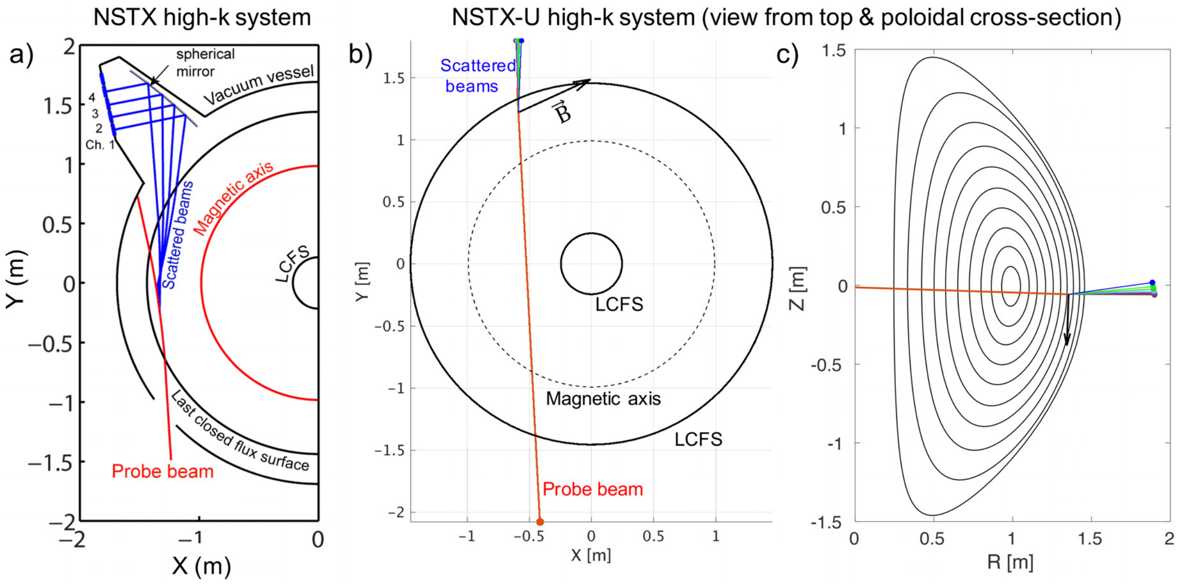

FIG. 9. (a) View from top of the NSTX high-k scattering geometry for 141767 [Reproduced from Phys. Plasmas **22**, 122501 (2015). Copyright 2015 AIP Publishing LLC]. The tangential geometry of this system was suited for performing high-k_r and lower k_θ wavenumber components of high-k turbulence. (b) View from top of the new NSTX-U high-k scattering geometry for the hypothetical scenario of shot 141767 (upward scattering). (c) Poloidal cross section of the new high-k scattering geometry for 141767. The new geometry of the probe and scattered beams allows for higher k_θ measurements than in the NSTX high-k system.

wavenumber spectrum. We adopt a Cartesian coordinate system (X, Y, Z) to describe the scattering geometry (Fig. 9), defining the corresponding wavenumber components (k_x, k_y, k_z) (these Cartesian coordinates do not correspond to those defined in Ref. 19. Details in Appendix A). We will also make use of the cylindrical coordinate system (R, Z, φ), where $R = \sqrt{X^2 + Y^2}$, $Z = Z$, and $\tan \varphi = Y/X$. The corresponding cylindrical wavenumber components (k_R, k_Z, k_φ) are defined in Sec. IV B and Appendix A.

The probe beam is launched with azimuthal angle of 93° (with respect to the X-axis on the X-Y plane) and polar angle of 91° (inclination angle with respect to the Z-axis). The launching point is $(X, Y, Z) = (-0.4147, -2.00809, 0)$ m, and the collection points are assumed to be at $Y = 1.8$ m [Figs. 9(b) and 9(c)]. The scattering location takes place at $R \approx 135$ cm, $Z \approx -6$ cm (corresponding to a poloidal angle $\theta \approx -4°$). Modeling the probe and scattered ray trajectories with a ray-tracing code shows negligible ray refraction takes place in the current conditions, given the high frequency $f_i = 693$ GHz of propagation with respect to the electron plasma and cyclotron frequencies ($f_{pe} \lesssim 70$ GHz, $f_{ce} \sim 20$ GHz). Projections of the scattering location and wavenumber components differ by less than 1% with respect to modeling the probe and scattered beams by straight line trajectories. As a result, the projections presented here are based on straight line trajectories of the probe and scattered beams. Note the high-k scattering system in NSTX exhibited non-negligible refraction due to the propagation geometry and reduced frequency $f_i = 280$ GHz [Fig. 9(a)], meaning ray-tracing was mandatory.

The selection of the turbulent wave-vectors $\vec{k}_+$ is dictated by the selection rules $\vec{k}_+ = \vec{k}_s - \vec{k}_i$, $\omega = \omega_s - \omega_i$ between the incident i, scattered s and selected turbulence wave-vectors and frequencies $(\vec{k}_i, \omega_i)$, $(\vec{k}_s, \omega_s)$, and $(\vec{k}_+, \omega)$.[35–39] The anisotropic nature of turbulent fluctuations imposes the constraint $\vec{k}_+ \cdot \vec{B} = 0$ to be satisfied by scattering experiments and will be imposed in the k-selection schemes that follow. Additionally, the condition for coherent scattering $|\vec{k}_+|\lambda_{De} \lesssim 1$ (Refs. 35–39) is largely satisfied in the present conditions.

With respect to spatial localization, the given scattering geometry suggests the vertical and toroidal dimensions of the scattering volume can be approximated by the beam waist a_0, giving $\Delta Z \approx R\Delta\varphi \approx a_0$. Radial localization is achieved by taking into account the anisotropy of the magnetic field and the scattering geometry.[40–42] Applied to the new high-k scattering geometry yields estimates $\Delta R \approx 5$ cm for $k_\perp = 10\ \text{cm}^{-1}$,[43] which is greatly enhanced from simple estimates based on the linear overlap volume between the incident and scattered beams. Typically ΔR decreases for increasing $k_\perp$. This justifies the use of local gyrokinetic simulations to predict the turbulence spectra for the new high-k scattering system. The diagnostic wavenumber resolutions $\Delta k_\theta \rho_s$ and $\Delta k_r \rho_s$ can be computed from knowledge of ΔZ and ΔR (Sec. IV B). A value of $\Delta Z \approx a_0 \approx 1.8$ cm leads to a spectral resolution $\Delta k_\theta \rho_s \approx 1.5$. A reference value of $\Delta R = 5$ cm leads to $\Delta k_r \rho_s \approx 0.06$ for the new high-k system.

B. Synthetic diagnostic for high-k scattering

In this subsection, we briefly describe the implementation of synthetic high-k diagnostics using local gyrokinetic simulation and GYRO/CGYRO notation. This builds on previous development of synthetic diagnostics for beam emission spectroscopy and correlation electron cyclotron emission,[44] Doppler backscattering,[45] and high-k scattering[46] using gyrokinetic simulation. The description presented is applied to the NSTX (documented in detail in Ref. 19) and NSTX-U high-k scattering diagnostics. Other high-k diagnostics could also be modeled using the synthetic description presented here, provided that the scattering volume ΔV could be written in separable form

$\Delta V \approx \Delta R\, \Delta Z\, R\Delta\varphi$. Specifics about the high-k scattering geometry are encapsulated in the selected wavenumber $\vec{k}_+$ and the spatial resolutions ΔR, ΔZ, and $R\Delta\varphi$, which will vary from system to system. The present description could also readily be adapted to other gyrokinetic codes using the corresponding internally defined wavenumber grid, ρ_s normalization, etc.

The synthetic diagnostic takes as input the raw simulated electron density fluctuating field $\delta n(k_r, k_\theta, \theta, t)$, the selected $\vec{k}_+$ by high-k scattering, and the diagnostic resolutions in the radial ΔR, vertical ΔZ, and toroidal $R\Delta\varphi$ directions. *A posteriori* filtering of the GYRO simulated raw density fluctuation field around $\vec{k}_+$ yields the synthetic density fluctuation signal $\delta n_{\mathrm{U}}(\vec{k}_+, t)$, which is used for the computation of spectra (details in Refs. 18 and 19). Here we characterize the measured $\vec{k}_+$ and the diagnostic resolutions that are fed into the synthetic diagnostic.

Ray-tracing (or beam tracing or equivalent calculations) provides the measured wavenumber components in cylindrical coordinates (k_R, k_Z, k_φ) (Appendix A), whereas gyrokinetic codes employ field-aligned geometry with perpendicular coordinates (k_r, k_θ) in the case of GYRO and CGYRO. The wavenumber components $(k_r, k_\theta)_+$ of the selected wave-vector are computed from the cylindrical components $(k_R, k_Z)_+$ via the following wavenumber mapping:[19]

$$\begin{aligned} k_{r+} - \frac{r}{q}\frac{\partial\alpha}{\partial r} k_{\theta+} &= \frac{\partial R}{\partial r} k_{R+} + \frac{\partial Z}{\partial r} k_{Z+} \\ -\frac{1}{q}\frac{\partial\alpha}{\partial\theta} k_{\theta+} &= \frac{1}{r}\frac{\partial R}{\partial\theta} k_{R+} + \frac{1}{r}\frac{\partial Z}{\partial\theta} k_{Z+}, \end{aligned} \tag{1}$$

where the geometric quantities r and q (safety factor) are evaluated locally, as well as the r and θ derivatives of the field-line label $\alpha = \alpha(r, \theta)$ and the flux-surface shape functions $R(r, \theta)$ and $Z(r, \theta)$. The cylindrical components of the wave-vector $\vec{k}_+ = (k_R, k_Z, k_\varphi)$ correspond to the projections of $\vec{k}_+$, respectively, along major-radius R, vertically Z, and along the toroidal direction φ. Formula 1 assumes that the cylindrical k_{R+} and k_{Z+} components only represent the central ray of the probing beam and do not vary with toroidal angle. Strictly speaking, a third equation corresponding to mapping the $k_{\varphi+}$ component should be appended to Eq. (1), namely, $-\frac{r}{qR} k_{\theta+} = k_{\varphi+}$. When the scattering condition $\vec{k}_+ \cdot \vec{B} \approx 0$ is well satisfied, the k_φ equation is redundant and the mapping is completely determined by Eq. (1). When $\vec{k}_+ \cdot \vec{B} \approx 0$ is not well satisfied, misalignment occurs which can be described via different selected $k_{\theta+}$ from Eq. (1) and the k_φ equation. As shown in Ref. 19, the toroidal direction introduces no additional effect on the filtering for essentially all $\Delta\varphi$ for well-aligned NSTX high-k scattering measurements. Additionally, the condition $\vec{k}_+ \cdot \vec{B} = 0$ will be imposed from the outset for the new high-k scattering system in NSTX-U. As a result, we use a 2D synthetic diagnostic in the R and Z plane which neglects toroidal variation (equivalent to $\Delta\varphi \to 0$) where the toroidal wavenumber component k_φ is absent in the description. A different coordinate system would need to be used to correctly incorporate 3D geometry (Ref. 19 and Appendix A). The full mapping including the k_φ equation could be employed to assess the effect of misalignment on the scattering amplitude, but is not the object of the present study.

The measurement range of three high-k scattering channels from shot 141767 is represented in Fig. 12(a) by three white dots on top of the raw GYRO spectral density $S(k_r, k_\theta) \propto |\delta n(k_r, k_\theta)|^2$ at the outboard midplane ($\theta = 0$) corresponding to the strong ETG condition. These correspond to a measurement of $k_r\rho_s \approx 2-3$ and $k_\theta\rho_s \approx 3-5$ (recall ρ_s uses the B_{unit} convention[12,26]). The density fluctuation wavenumber spectrum is anisotropic in (k_r, k_θ), peaking at finite $k_r\rho_s \approx -1$ and $k_\theta\rho_s \approx 4-8$. This corresponds to tilted, radially elongated eddies known as ETG streamers.[5,6] The additional colored dots around the streamer peak in Fig. 12 correspond to potential high-k measurements in NSTX-U. The spectral density in Fig. 12(a) has been averaged during the turbulent saturated phase of the gyrokinetic simulation (during a time period ≈14 a/c$_s$).

The selected $\vec{k}_+$ can be interpreted as the wave-vector providing the dominant contributions to the scattered signal. A range of wave-vectors centered around $\vec{k}_+$ also contribute to the measured fluctuation power depending on the wavenumber resolution of the diagnostic. The dimensions of the scattering volume in the radial ΔR and vertical ΔZ determine the diagnostic wavenumber resolutions Δk_r and Δk_θ (the toroidal dimension $R\Delta\varphi$ is absent in the 2D description). These are well approximated by $\Delta k_r\rho_s \approx \frac{2}{|\nabla r|\Delta R}\rho_s$ and $\Delta k_\theta\rho_s \approx \frac{2\kappa q}{\Delta Z(\partial\alpha/\partial\theta)}\rho_s$ for $\theta \approx 0$ (Ref. 19) (here κ is elongation, while $\partial\alpha/\partial\theta$ and $|\nabla r|$ are functions characterizing the flux surface geometry. More details in Appendix B).

Fourier analysis of the synthetic signal $\delta n_{\mathrm{U}}(\vec{k}_+, t)$ yields the frequency power spectrum of fluctuations, represented by the spectral density $S(\vec{k}_+, \omega) = \frac{1}{TV_s}\langle\frac{|\delta n_{\mathrm{U}}(\vec{k}_+,\omega)|^2}{n_0}\rangle$. Here T is the collection time, n_0 is the background density, and the brackets denote an ensemble average. This quantity can be directly compared to the measured high-k frequency spectrum [Fig. 3(a)]. The density fluctuation wavenumber power spectrum $S(\vec{k}_+)$ can be computed from the frequency power spectrum $S(\vec{k}_+, \omega)$ via integration within a prescribed frequency band (as in experiment) and can be directly compared to the measured high-k wavenumber spectrum [Fig. 3(b)].

C. Potential routes for high-k measurements

With views of sampling the high-k density fluctuation wavenumber power spectrum, we introduce two different schemes designed to predominantly measure the poloidal k_θ and radial k_r wavenumber dependence of the spectrum around the streamer peak. These projections assume that a full suite of eight scattering channels are available for a given experiment.

For each case, we use $\vec{k}_+ = \vec{k}_s - \vec{k}_i$ to select a turbulence wavevector $\vec{k}_+$ expressed in Cartesian coordinates. Following the procedure outlined in detail in Refs. 18 and 19, we map $\vec{k}_+$ to the components (k_r, k_θ) employed by GYRO/CGYRO using Eq. (1) (the Cartesian coordinates defined here do not correspond to those in Ref. 19. Details in Appendix A). In the present 2D description, we use the dimensions of the scattering volume in the radial ΔR and vertical ΔZ directions to define the filter functions applied on the turbulence amplitude δn via the synthetic diagnostic. For each set of $\vec{k}_+$, we then deploy the synthetic diagnostic to the output of a nonlinear gyrokinetic simulation that scanned $(\nabla n, q, \text{and } \hat{s})$ from their experimental values, one of the two that best matched all the experimental observables in Sec. II. The frequency $S(k_{r+}, k_{\theta+}, \omega)$ and wavenumber spectra $S(k_{r+}, k_{\theta+})$ are computed following the details from Sec. IV B.

Published under license by AIP Publishing

1. Measuring the k_θ dependence of the spectrum

In order to scan the k_θ dependence of the turbulent wavenumber spectrum we perform scans in the vertical Cartesian coordinate k_z. This is a good approximation since the projected measurements are made near the outboard equatorial plane (for $\theta = 0$ the second equation in Eq. (1) reduces to $k_{\theta+} = -\kappa q/(\partial\alpha/\partial\theta)k_{z+}$). In order to scan k_z, we work in Cartesian coordinates to perform the following procedure for selecting $\vec{k}_+$: (1) choose a particular value of $k_\perp$ (cm^{-1}), (2) choose a particular k_y component, and (3) use $\vec{k}\cdot\vec{B} = 0$ to solve for the corresponding k_x and k_z components (select $k_z > 0$ for upwards scattering). Once a particular k_z is found, we iterate for different $k_\perp$, which will select different k_z (and k_x) keeping k_y fixed. In addition to scanning k_z, this procedure also introduces a different k_x component for each iteration. This translates to a small but finite k_r in the field-line following frame [Eq. (1) reduces to $k_r \approx k_R/|\nabla r|$ for $\theta \approx 0$, which contains a k_x dependence]. Introducing a small but finite k_r is desired in plasma conditions with strong flow shear since the peak of the spectrum is expected to take place at a finite k_r, helping us probe the wavenumber spectrum as close as possible to the streamer peak. The streamer peak for the particular case study presented here takes place at $k_r\rho_s \approx -1$. An example of selected $\vec{k}_+$ using this k_θ-scanning procedure is schematically shown by the red dots overlaid on the simulated spectral density $S(k_r, k_\theta)$ in Fig. 12(a).

In Figs. 10(a) and 10(b) are shown views from the top and poloidal cross section of the probe and scattered beams issued by the previous procedure for k-selection. The selected $\vec{k}_+$ (colored arrows) are scaled by a constant for visualization purposes. The black arrow shows the magnetic field projection on each plane. The varying $\vec{k}_+$ are all perpendicular to $\vec{B}$ by design and primarily scan k_z. Mapped to the $(k_r\rho_s, k_\theta\rho_s)_+$ components in GYRO/CGYRO, these correspond to $k_{\theta+}\rho_s \approx [2-30]$ while $k_{r+}\rho_s \approx -1$ (the specific values are given on Appendix B). In Fig. 10(c) are shown the corresponding frequency spectra issued from deployment of the synthetic high-k diagnostic for the different $\vec{k}_+$. Even a moderate Mach number ($M \approx 0.18$) produces a Doppler shift ω_D that is ∼2 orders of magnitude larger than the plasma frame frequency of fluctuations. The peak of the frequency spectrum is shifted up to frequencies of $f \approx -10$ MHz for the higher k_θ components, and is shown to roughly follow the Doppler shift frequency $\omega_D = \vec{k}_+ \cdot \vec{v} \propto (r/qR)Mk_{\theta+}$. Higher frequencies would be expected for measurements with higher $k_{\theta+}$ and higher Mach number M. The amplitude of the fluctuations spans three orders of magnitude in power, and is shown to decrease for increasing $k_{\theta+}$, while the width of the spectrum becomes wider for increasing $k_{\theta+}$.

Figure 12(b) shows the power of the synthetic spectral density $S(k_{r+}, k_{\theta+})$ for the eight selected wavenumbers $\vec{k}_+$ by the k_θ-scanning procedure. These correspond to the red dots on Fig. 12(a). The amplitude of the synthetic spectral density peaks at wavenumbers $k_\theta\rho_s \approx 5-6$ ($k_\theta\rho_e \approx 0.1$), and decays with a power-law dependence for higher k_θ characteristic of turbulence in the inertial range of the cascade. A power-law fit to the spectrum reveals $|\delta n|^2 \propto k_\theta^{-3.84}$. Future measurements of the peak of the spectrum and the spectral exponent in k_θ could prove critical for validating existing turbulent theories and could serve as potential observables in future validation studies.

2. Measuring the k_r dependence of the spectrum

Here we design a scheme to probe the k_r dependence of the density fluctuation power spectrum. We perform two sets of scans focusing separately on positive $k_r > 0$ vs negative $k_r < 0$. By separately covering ($k_\theta > 0$, $k_r > 0$) and ($k_\theta > 0, k_r < 0$), we ensure full coverage of the spectrum in k_r and k_θ around the streamer peak [the negative k_θ can be computed by the reality condition $\delta n(-k_r, -k_\theta) = \delta n(k_r, k_\theta)^*$].

We propose to sample the k_r dependence of the spectrum using the following k-selection procedure: (1) choose a particular $k_\perp$ (cm^{-1}),

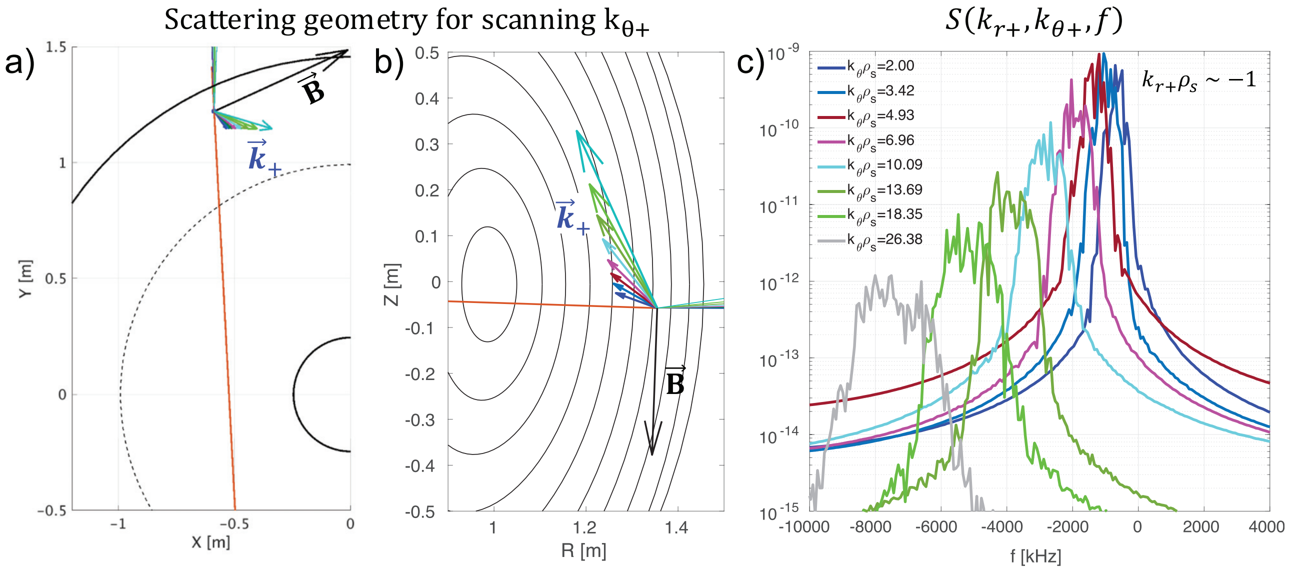

FIG. 10. (a) View from the top of the probe and scattered beam trajectories for measuring the dependence in k_θ of the density fluctuation spectrum. (b) Poloidal cross section on the (R, Z) plane corresponding to the geometry in (a). Colored arrows represent the measured $\vec{k}_+$ for each scan. (c) Frequency spectra computed via synthetic high-k diagnostic corresponding to the wave-vectors in (a) and (b).

Published under license by AIP Publishing

(2) choose a particular $k_z > 0$ component (upwards scattering), and (3) use $\vec{k} \cdot \vec{B} = 0$ to solve for the corresponding k_x and k_y components. Once particular k_x and k_y are found, we can iterate the procedure for different $k_\perp$ which will select different k_x and k_y while keeping k_z fixed (negative $k_r < 0$ corresponds to $k_y < 0$, while $k_r > 0$ corresponds to $k_y > 0$). This procedure results in scanning primarily k_R (and subsequently k_r) while introducing small variations in k_θ. A fixed $k_z = 4\,\mathrm{cm}^{-1}$ component is chosen to probe the spectrum around the streamer peak given by $k_\theta \rho_s \approx 5 - 6$.

Figures 11(a) and 11(b) show a view from the top and poloidal cross section of the probe and scattered beams and the corresponding selected $\vec{k}_+$ having $k_{r+} < 0$. The selected $\vec{k}_+$ are scaled by a constant for visualization purposes (colored arrows). Note how this procedure primarily scans the radial k_R component. The mapped radial wavenumber components range from $k_r \rho_s \,\epsilon\, [-6, 0]$. This $\vec{k}$-selection procedure introduces variations in the poloidal wavenumber in the range $k_\theta \rho_s \approx [2, 5]$. This might appear counter-intuitive since the same k_z is selected for each of the eight wave-vectors $\vec{k}_+$ [the second equation in Eq. (1) reduces to $k_{\theta+} = -\kappa q/(\partial\alpha/\partial\theta) k_{z+}$ for $\theta = 0$ implying $k_{\theta+}$ should be constant for fixed k_{z+}]. The variation in $k_{\theta+}$ is in fact due to the off-midplane corrections to the previous formula, suggesting the mapping given by Eq. (1) should be employed even for small off-midplane locations as small as $\theta_0 \approx -4°$ presently. This is due to the effect of the $\partial R/\partial\theta$ term in Eq. (1), which is enhanced for large k_R and in strongly shaped plasmas such as in spherical tokamaks. A similar conclusion was reached in Ref. 19 when mapping to k_r and k_θ for the high-k scattering diagnostic in NSTX. Figure 11(c) shows the frequency spectra computed via synthetic diagnostic corresponding to each of the selected $\vec{k}_+$ in Figs. 11(a) and 11(b). Even though small variations are introduced in k_θ, the frequency spectrum here does not exhibit as wide variation in the frequency range as in the previous scan in k_θ and now peaks between $f \approx -(1-2)$ MHz for all selected $\vec{k}_+$. The amplitude of the fluctuation spectrum span around three orders of magnitude, while no appreciable variation is observed in the width of the frequency spectrum for the different k_{r+}.

The selected $(k_r, k_\theta)_+$ components are overlaid on the 2D wavenumber spectrum in Fig. 13(a) and depicted by the blue dots. One can visually see the peak of the spectrum appears to have been sampled following this procedure to scan $k_r < 0$. In Fig. 12(c) is shown the amplitude variation of the synthetic spectral density $S(k_{r+}, k_{\theta+})$ for the eight selected wavenumbers $\vec{k}_+$ by the k_r-scanning procedure. The blue dots correspond to those in Fig. 12(a), and show a peak in the spectrum around $k_{r+}\rho_s \approx -1$. For higher values of k_r the spectrum is shown to exhibit a power-law dependence characteristic of the inertial range in the turbulent cascade, here given by $|\delta n|^2 \propto k_r^{-4.3}$ for $|k_{r+}\rho_s| > 1$. Note the span in k_{r+} is $k_{r+}\rho_s \,\epsilon\, [-6, -0.1]$ is a smaller range than in $k_\theta \rho_s \,\epsilon\, [2, 30]$. The peak of the spectrum and the spectral index in k_r could be relevant observables to validate existing turbulent theories against future high-k measurements.

The peak of the spectrum at finite k_r is evidence of an asymmetric spectrum. In fact, the density fluctuation wavenumber power spectrum $S \propto |\delta n(k_r, k_\theta)|^2$ is expected to be asymmetric in k_r in the presence of a symmetry breaking mechanism.[47] Here the inclusion of perpendicular $E \times B$ and parallel flow shear in the nonlinear gyrokinetic simulations break an underlying symmetry in the gyrokinetic equation leading to an asymmetric spectrum in k_r. The peak of the spectrum for a finite k_r also introduces a tilt of the turbulent eddies in the perpendicular direction,[48] and has previously been observed in nonlinear gyrokinetic simulations of ETG in NSTX[49] and MAST.[50] These projections suggest that high-k scattering could provide experimental evidence of such an asymmetry.

The same procedure is performed to probe the $k_r > 0$ parts of the density fluctuation wavenumber power spectrum. Figures 13(a) and 13(b) show a view from the top and poloidal cross section of the

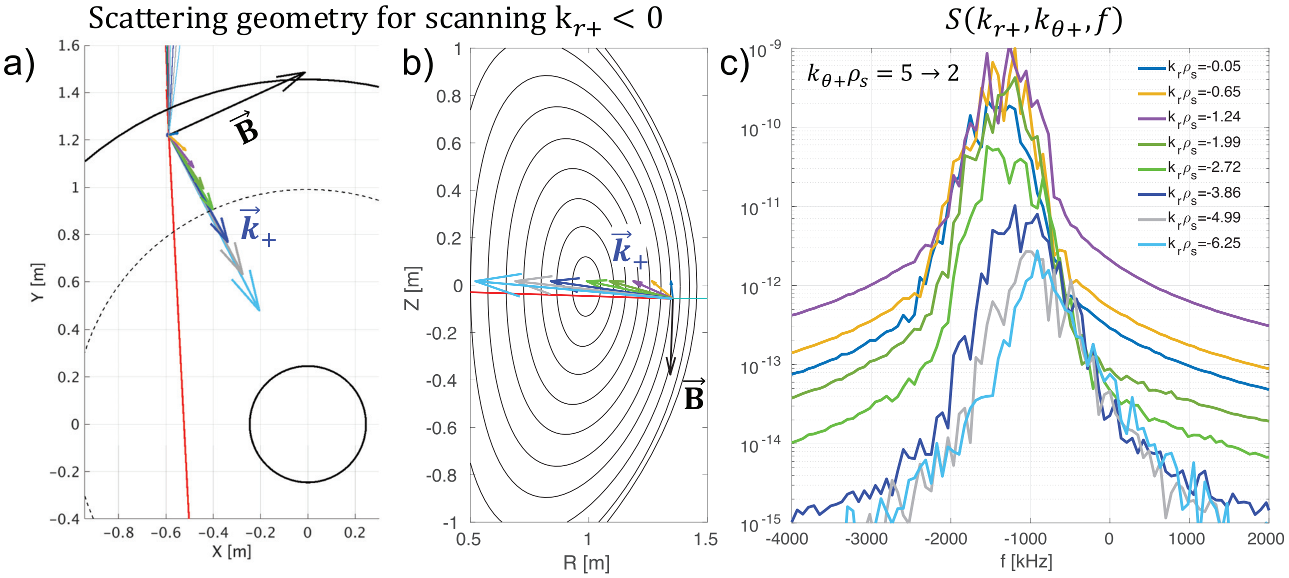

FIG. 11. (a) View from the top of the probe and scattered beam trajectories for measuring the dependence of the density fluctuation spectrum for $k_r < 0$. (b) Poloidal cross section on the (R, Z) plane corresponding to the geometry in (a). Colored arrows represent the measured $\vec{k}_+$ for each scan. (c) Frequency spectra computed via synthetic high-k diagnostic corresponding to the wave-vectors in (a) and (b).

Published under license by AIP Publishing

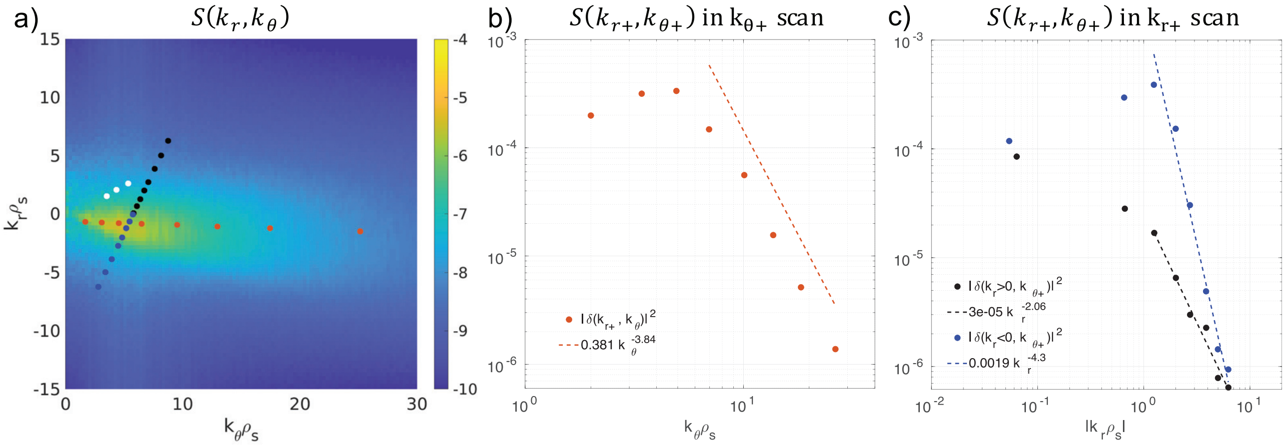

FIG. 12. (a) 2D wavenumber spectrum of the electron density $S(k_r, k_\theta) \propto |\delta n(k_r, k_\theta)|^2$ at the outboard midplane. White dots indicate the high-k measurement range for 141767 in NSTX, while red, black, and blue dots are projections for potential measurements with the new high-k system in NSTX-U. (b) Dependence of the synthetic spectrum $S(k_{r+}, k_{\theta+})$ with k_θ in a projected scan in $k_{\theta+}$. (c) Dependence of the synthetic spectrum $S(k_{r+}, k_{\theta+})$ with k_r in projected scans for $k_{r+} > 0$ and $k_{r+} < 0$.

probing, scattered and selected $\vec{k}_+$ characterized by $k_{r+} > 0$, while Fig. 13(c) shows the corresponding frequency spectra. Once more a small variation is introduced in k_θ due to the high k_R values and off-midplane corrections. This time k_r is scanned from $k_r\rho_s \,\epsilon\, [0.1, 6]$, while k_θ is in the range $k_\theta\rho_s \approx [5, 8]$. The peak power of the frequency spectra spans two orders of magnitude and peaks at frequencies $f \approx -(1-2)$ MHz. The frequency peak is again shown to be proportional to the selected $k_{\theta+}$, while no significant variation can be observed in the spectral width with $k_{r+} > 0$.

The selected $\vec{k}_+$ having $k_{r+} > 0$ are plotted by black dots over the 2D wavenumber spectrum in Fig. 13(a). The corresponding variation of the spectral power $S(k_{r+}, k_{\theta+})$ with $k_{r+} > 0$ is given in Fig. 13(c) by the black dots. Note this time no peak is observed for positive $k_r > 0$, and the spectrum is shown to monotonically decrease. A power-law $|\delta n|^2 \propto k_r^{-2.06}$ can be fit to the spectrum for $k_r\rho_s \gtrsim 1$, a factor of two shallower than for negative $k_r < 0$ (note however the applicable range is $|k_r\rho_s| \lesssim 6$). The asymmetry with respect to the peak of the spectrum and spectral exponent in k_r could possibly be quantifiable in future scattering experiments.

We note that the values of the metrics presented here (peak of the spectrum and spectral indices in k_r, k_θ) are not affected by the synthetic diagnostic. The observable values issued from the synthetic

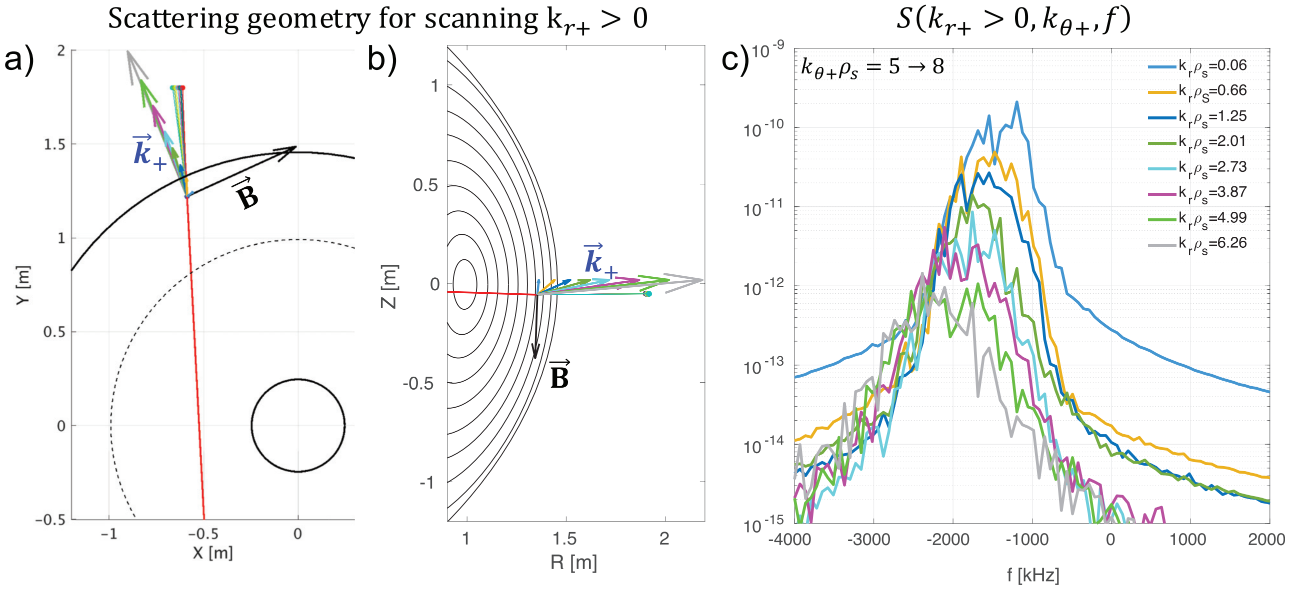

FIG. 13. (a) View from the top of the probe and scattered beam trajectories for scanning the measuring the dependence of the density fluctuation spectrum for $k_r > 0$. (b) Poloidal cross section on the (R, Z) plane corresponding to the geometry in (a). Colored arrows represent the measured $\vec{k}_+$ for each scan. (c) Frequency spectra computed via synthetic high-k diagnostic corresponding to the wave-vectors in (a) and (b).

Published under license by AIP Publishing

diagnostic are in agreement with the corresponding values of the peak and spectral indices computed from raw density fluctuations taken as direct output from nonlinear gyrokinetic simulation.

V. CONCLUSIONS

In summary, in this article, we have reviewed previous validation work of nonlinear electron-scale gyrokinetic simulations via comparisons of density fluctuation spectra between experiment and simulation;[18] we have discussed the potential role that the ion-scale instability and turbulence might play on the weakly driven ETG condition and used the strongly driven ETG condition to project future high-k measurements in NSTX-U.

Section II constitutes a succinct review of Refs. 18 and 19 and has given extensive experimental evidence supporting the thesis of ETG-driven turbulence as the main responsible driver of anomalous electron thermal transport in the outer core-gradient region of a modest-β NSTX NBI-heated H-mode. These conclusions are reached after performing detailed comparisons of electron thermal transport and measured high-k density fluctuation spectra between experiments and simulation. These have shown that the anomalous levels of electron thermal power can be reproduced by nonlinear electron-scale gyrokinetic simulation in conditions where high-k density fluctuations measured by high-k scattering were both low and high (respectively, alluded to weak and strong ETG drive times). Simulations were simultaneously able to reproduce the shape of the measured high-k wavenumber spectrum, as well as the ratio of fluctuation levels between strongly driven and weakly driven ETG turbulence conditions. As concluded in Ref. 18, this provides the strongest experimental evidence to date supporting ETG-driven turbulence as a main driver of anomalous electron thermal transport in the outer core of a modest-β ST plasma.

One important comment should be made with respect to the role of ion-scale turbulence, presented in Sec. III. For the strong ETG condition, it was shown in Ref. 18 that ion-scale turbulence cannot be destabilized within uncertainty in the turbulence drive terms. This is consistent with the maximum linear growth rate lying clearly below the background $E \times B$ shearing rate (Fig. 4). For the weak ETG condition, the situation is more subtle. We summarize the most important evidence for the weak ETG condition: (1) the measured high-k fluctuation power is lower than for the strong ETG condition, (2) ion thermal transport is very close to the neoclassical levels predicted by NEO,[23] and (3) nonlinear electron-scale gyrokinetic simulation can reproduce electron thermal power within uncertainty in ∇T and ∇n (shown in Ref. 18). This evidence allowed us to conclude that ion-scale turbulence drives negligible electron thermal transport for the weak ETG condition. However, as shown in Sec. III A, the ion-scale instability lies very close to the linear KBM threshold (β^{crit}). Additionally, Sec. III B shows that ion-scale turbulence may be very close to the nonlinear threshold in a state possibly reminiscent of the Dimits-shift regime.[29] Within experimental uncertainty in the turbulence drives ($\nabla T, \nabla n$) a TEM/KBM mode can be excited and lead to unphysically large ion and electron thermal powers.

These findings bring into question the role that the ion-scale instability and turbulence might play at the weak ETG condition. We argue, however, that it is unlikely that ion-scale turbulence might impact our conclusions since the constraints presented mainly concern the strong ETG condition for which we are confident that ion-scale turbulence is suppressed. It is possible, however, that the fluctuation level ratio might be affected by the presence of ion-scale turbulence in the weak ETG regime. This remains speculative owing to the neoclassical ion thermal transport levels: ion-scale turbulence would need to drive electron thermal transport but negligible ion thermal transport in order to comply with the neoclassical ion thermal transport constraint, but it remains a possibility. If this were true, the presence of ion-scale turbulence driving electron thermal transport for the weak ETG condition would imply a lower value of electron-scale electron thermal transport, which would increase the fluctuation level ratio presented with the current simulations (recall the fluctuation level ratio is between the strong and weak ETG drive). This might mean that the experimental value of the fluctuation level ratio could be matched at lower turbulence drives for the strong ETG condition. Additional simulations would need to be performed to confirm this speculation.

One additional possibility concerning the role of ion-scale turbulence is multi-scale interactions between ion-scales and electron-scales, which cannot be ruled out for the weak ETG condition. In fact, recent work[51] has shown that the electron thermal power can be greatly enhanced via cross-scale interactions in conditions where ion-scale turbulence is close to the nonlinear threshold: a very similar situation to the weak ETG condition, as shown in Secs. III A and III B. This discussion also shows one weakness of the present work, namely, the lack of experimental constraint on ion-scale turbulence and further motivates the simultaneous use of multi-scale diagnostics in future validation studies.

Successfully validated nonlinear gyrokinetic simulations of ETG-driven turbulence are used to project high-k turbulence spectra by the new high-k scattering system in NSTX-U. Here no assessment is made on the practicality of the measurements, and it is possible that future measurements inspired by the high-k projections made will be challenging or even unfeasible. If experimentally feasible, they could guide future high-k turbulence studies in NSTX-U. Hypothetical measurements of the peak of the high-k fluctuation wavenumber spectrum and the spectral indices in k_r and k_θ could reveal experimental evidence of the anisotropy in the 2D (k_r, k_θ) spectrum of high-k turbulence, the tilt of turbulent eddies in the perpendicular direction to $\vec{B}$ (and the associated breaking of symmetry[47,48]) and, maybe most importantly, the first experimental demonstration of the presence of radially elongated and poloidally thin streamer fluctuations, which to the best of our knowledge, remain elusive to present. Inspired by previous works,[52–55] we have identified the peak of the density fluctuation wavenumber spectrum in k_θ and k_r and the spectral indices in k_θ and k_r as critical validation metrics on the turbulence that could be used to validate future electron-scale gyrokinetic simulations. Turbulence characteristics, as well as turbulence fluxes, should be matched in order to fully validate our current turbulence and transport models. This in turn will guide the development of synthetic diagnostics, which yield a profound understanding toward the interpretation of fluctuation measurements. High-k measurements in NSTX-U will be possible from the core $r/a \approx 0.1$ to the pedestal at $r/a \approx 0.99$, and in higher performance plasmas, which will reveal intrinsic characteristics of the underlying turbulence in yet unexplored parameter regimes to date.

Care should be taken to extrapolate the results shown here to higher performance ST scenarios in the upcoming NSTX-U and MAST-U as well as for future reactors based on the ST concept, both from the machine specifications and the expected nature of the turbulence. Machine specifications such as doubling of the magnetic field in

NSTX-U could decrease the size of the turbulent structures since their characteristic length scales with ρ_s ($\rho_s \sim T_e^{1/2}/B$). Although higher temperatures will likely be reached in full-field NSTX-U experiments, T_e will need to increase fourfold in order to maintain the same ρ_s as in NSTX. Assuming the turbulence characteristics unchanged, full-field NSTX-U experiments are likely to exhibit smaller ρ_s values, translating to smaller ion and electron-scale turbulent structures, i.e., characterized by higher $k_\perp$ (m^{-1}). Another factor impacting the measured values of k_r and k_θ is the flux surface geometry. Equation (1) shows how the flux-surface geometry can impact the mapped k_{r+} and $k_{\theta+}$ for a given $\vec{k}_+$. For clarity, Eq. (1) is simplified at the outboard midplane to $k_{r+} \approx k_{R+}/|\nabla r|$ and $k_{\theta+} \approx -\kappa q/(\partial\alpha/\partial\theta)k_{z+}$, showing how $|\nabla r|$ [related to Shafanov shift $|\nabla r| \approx 1/(1+\Delta)$] and κ (elongation) can strongly impact the measurement at the outboard midplane, in particular, for strongly shaped plasmas such as STs (and will also vary radially). However, the high-k scattering capabilities for NSTX-U should comfortably allow the measurement of even smaller streamer structures than those presented here, due to the large spectral range in k accessible [$k_\perp > 40\ \mathrm{cm}^{-1}$ (Ref. 27)]. Sampling the k_r spectrum might be most limiting factor in future experiments (recall the spectral range for the present projections is $|k_r\rho_s| \lesssim 6$ while $k_\theta\rho_s \lesssim 27$, Appendix B), but the spectral peak at $k_r\rho_s \approx -1$ and $k_\theta\rho_s \approx 5-6$ should comfortably be accessible in NSTX-U.

Care should also be taken to extrapolate the present high-k projections to higher performance plasmas accessing different turbulence regimes. NSTX H-mode 141767 is a relatively low β, modest collisionality spherical tokamak plasma. Ion-scale turbulence was stabilized by strong $E \times B$ shear and ETG was the dominant electron heat transport mechanism. However, as mentioned in Sec. I and in Fig. 1, the kinetic ballooning mode and micro-tearing modes are predicted to be the dominant instability in higher β regimes. High performance ST plasmas will also have lower collisionality, which following Fig. 1 would point to the kinetic ballooning mode as the dominant instability predicted in high performance ST scenarios. The presence of electron-scale turbulence in a different turbulent regime might peak at different $k_r\rho_s$ and $k_\theta\rho_s$ values, which would have implications in the measurement (e.g., more weakly driven ETG turbulence would likely exhibit smaller eddies, i.e., higher $k_\perp$). The presence of electromagnetic turbulence also motivates further work to detect electromagnetic modes in NSTX-U and MAST-U devices, using diagnostics such as polarimetry, cross-polarization scattering, or additional techniques.

Further down the road, the goal is to predict equilibrium plasma profiles of future high performance ST reactors. This work serves as a stepping stone to understanding electron thermal transport, but more emphasis should be placed on developing reliable predictive transport simulations coupled with reduced transport models such as TGLF,[56] which is still at its early stage for the spherical tokamak. Developing reduced transport models accurate to the high beta, high flow, and low-aspect ratio ST regime should be a main research priority of future confinement studies in NSTX-U and MAST-U. These efforts would drive the prediction and optimization of the performance of future fusion ST reactors.

ACKNOWLEDGMENTS

The author would like to thank the whole NSTX team for providing the profile data used for the analysis of the plasma discharge presented here. This work was supported by U.S. D.O.E. Contract No. DE-AC02-09CH11466 and in part by the Engineering and Physical Sciences Research Council (EPSRC) [EP/R034737/1]. Computer simulations were carried out at the National Energy Research Scientific Computing Center, supported by the Office of Science of the U.S. D.O.E. under Contract No. DE-AC02-05CH11231, and at the MIT-PSFC partition of the Engaging cluster at the MGHPCC facility (www.mghpcc.org), which was funded by D.O.E. Grant No. DE-FG02-91-ER54109. N.F.L. was partially funded by U.S. D.O.E. Grant No. DE-FG02-91ER54109. The digital data for this paper can be found in http://arks.princeton.edu/ark:/88435/dsp011v53k0334.

APPENDIX A: RELATION TO SYSTEMS OF REFERENCE IN PAST WORK

In this appendix, we clarify the difference in coordinates and notation employed for the synthetic diagnostic throughout this manuscript with respect to a previous publication.[19]

In Ref. 19, the synthetic diagnostic was described in terms of a mapping between wavenumber components written in a Cartesian coordinate system $(k_x, k_y, k_z)_+$ [noted $(k_x, k_y, k_z)_+$ (Ref. 19) in what follows] mapped to toroidal and radial mode numbers $(n, p)_+$ in GYRO [Eq. (8) in Ref. 19]. We emphasize that the Cartesian coordinates from Eq. (8) in Ref. 19 do not correspond to the Cartesian coordinates defined here. In Ref. 19, the Cartesian components employed a Cartesian system centered at the scattering location, where k_x (Ref. 19) was along the major radial direction, k_y (Ref. 19) was along the toroidal direction, and k_z (Ref. 19) along the vertical direction. In the case of the 2D description of the synthetic diagnostic [in the (R, Z) plane], these are, respectively, equivalent to the k_R, k_φ, and k_Z components defined here. However, special care must be taken when implementing the 3D version of the synthetic diagnostic including toroidal variation. The cylindrical coordinate system varies with toroidal angle, which introduces variations in the (k_R, k_φ, k_Z) components for a fixed $\vec{k}_+$. Using fixed $k_{R+}, k_{\varphi+}$, and k_{Z+} components in the synthetic diagnostic would result in selecting a different $\vec{k}_+$ in different toroidal locations, which would be inconsistent. Using the Cartesian coordinate system from Ref. 19 alleviates this issue. However, in the limit of the 2D synthetic diagnostic description, both coordinate systems are strictly the same.

Throughout this manuscript, the Cartesian components (k_x, k_y, k_z) correspond to a Cartesian system centered at the center of the tokamak domain, where k_x, k_y, and k_z are the $\vec{k}$-components along the X, Y, and Z-directions, respectively (Fig. 9), and should not be confused with the Cartesian coordinate system in Ref. 19. Figure D2(b) in Ref. 19 shows the Cartesian component definitions (k_x, k_y, k_z).[19]

With respect to the (n, p) mode numbers used in the synthetic diagnostic description in Ref. 19, these have a direct relationship to the (k_θ, k_r) defined in this manuscript, namely, $(k_\theta, k_r) = (\frac{nq}{r}, \frac{2\pi p}{L_r})$ where L_r is the radial box dimension of the gyrokinetic simulation.

APPENDIX B: DETAILS ABOUT THE SELECTED $\vec{k}$ IN NSTX-U PROJECTIONS

In this appendix, we provide additional details concerning geometry definitions and specific parameter values needed in the

Published under license by AIP Publishing

wavenumber mapping [Eq. (1)]. The values of $k_\perp$, the cylindrical components (k_R, k_Z, k_φ) and field-aligned (k_r, k_θ) components used in the projection scans for high-k scattering in NSTX-U are also included. These are related via Eq. (1), repeated here for reference

$$\begin{aligned} k_r - \frac{r}{q}\frac{\partial\alpha}{\partial r}k_\theta &= \frac{\partial R}{\partial r}k_R + \frac{\partial Z}{\partial r}k_Z \\ -\frac{1}{q}\frac{\partial\alpha}{\partial\theta}k_\theta &= \frac{1}{r}\frac{\partial R}{\partial\theta}k_R + \frac{1}{r}\frac{\partial Z}{\partial\theta}k_Z. \end{aligned} \tag{A2}$$

In Eq. (A2), $R = R(r,\theta)$ and $Z = Z(r,\theta)$ are the flux functions describing the shape of the flux surface. Here we employed the Miller flux surface parametrization.[26] $\alpha = \alpha(r,\theta)$ is the field-line label, related to the equilibrium magnetic field via $\vec{B} = \nabla\alpha \times \nabla\psi$, where ψ is poloidal flux divided by 2π. The functions R, Z and α can be computed numerically from knowledge of the magnetic equilibrium reconstruction such as provided by EFIT.

The first row of Table I shows the Miller geometry parameters $\kappa, s_\kappa, \delta, s_\delta, R_0/a, \Delta, q, \hat{s}, \beta^*$[26] necessary to reconstruct the flux surface functions $R(r,\theta), Z(r,\theta)$ (here we have chosen to provide $\beta^* = -8\pi/B_{\text{unit}}^2 \frac{dp}{dr}$ instead of α_{MHD}). The second row of Table I shows the radial and θ derivatives of R, Z and α necessary for the wavenumber mapping, along with the normalized minor radius r/a, the θ location of scattering θ_s and $|\nabla r|$ the gradient of r. The cylindrical coordinates of the scattering location are $R_s = 1.3547$ m, $Z_s = -0.05771$ m, and $\varphi_s = 115.71°$. Normalization parameters are $B_{\text{unit}} = 1.4461$ T, $\rho_s = 0.1975$ cm (using B_{unit}), $\rho_s^{\text{exp}} \approx 0.7$ cm, and $a = 0.6012$ m minor radius at the last closed flux surface.

Next we provide the set of values of $k_\perp$, the cylindrical wavevector components (k_R, k_Z, k_φ), and the mapped values to the field-aligned (k_r, k_θ) used for scanning the k_θ (Table II), $k_r < 0$ (Table III), and $k_r > 0$ dependence (Table IV) of the high-k wavenumber spectrum in Sec. IV of the main text. Since $k_\perp$ is intrinsically a local quantity defined by the measurement, in Tables II–IV $k_\perp$ is normalized to the local, experimental ρ_s^{exp} (using local B_T), which can prove useful for the experimental diagnostician. On the other hand, k_r and k_θ are normalized to ρ_s using B_{unit} as internally used in GYRO, consistent with making "apples-to-apples"

TABLE I. First row provides the Miller geometry parameters[26] necessary to reconstruct $R(r,\theta), Z(r,\theta)$: κ elongation, $s_\kappa = r\,d\ln(\kappa)/dr$, δ triangularity, $s_\delta = r d\delta/dr$, R_0/a aspect ratio, $\Delta = dR_0/dr$ Shafranov shift, q safety factor, $\hat{s} = (r/q)dq/dr$ magnetic shear, $\beta^* = -8\pi/B_{\text{unit}}^2 \frac{dp}{dr}$. Second row provides additional geometry parameters necessary in the wavenumber mapping [Eq. (A2)]: r/a normalized minor radius, θ_s poloidal angle of scattering location, along with r and θ derivatives of R, Z and α. $|\nabla r|$ is the gradient of r.

κ	s_κ	δ	s_δ	R_0/a	Δ	q	$\hat{s}$	β^*
2.1127	0.1540	0.2483	0.3240	1.5227	−0.3041	3.4103	2.1656	0.02167

r/a	θ_s(deg)	$\frac{\partial R}{\partial r}$	$\frac{\partial R}{\partial\theta}$	$\frac{\partial Z}{\partial r}$	$\frac{\partial Z}{\partial\theta}$	$\frac{\partial\alpha}{\partial r}$	$\frac{\partial\alpha}{\partial\theta}$	$\|\nabla r\|$
0.7084	−3.5552	0.6913	0.0427	−0.1512	0.9289	−0.2031	1.1551	1.4337

TABLE II. The set of wavenumber components used for scanning the k_θ dependence of the spectrum in Sec. IV. All $\vec{k}_+$ have a constant value of $k_y = -4\ \text{cm}^{-1}$.

Wavenumber components in k_θ scan								
$k_\perp$ (cm^{-1})	5.2	6	7	8.5	11	14	18	25
$k_\perp\rho_s^{\text{exp}}$	3.6	4.2	4.9	5.9	7.7	9.8	12.6	17.5
k_R (cm^{-1})	−4.83	−5.09	−5.38	−5.76	−6.35	−7.02	−7.90	−9.40
k_Z (cm^{-1})	1.76	2.87	4.04	5.62	8.07	10.86	14.50	20.75
k_φ (cm^{-1})	−0.80	−1.36	−1.94	−2.74	−3.96	−5.36	−7.18	−10.30
$k_r\rho_s$	−0.67	−0.70	−0.74	−0.79	−0.87	−0.96	−1.07	−1.26
$k_\theta\rho_s$	2.00	3.42	4.93	6.96	10.09	13.69	18.35	26.38

TABLE III. The set of wavenumber components used for scanning the $k_r < 0$ dependence of the spectrum in Sec. IV. All $\vec{k}_+$ have a constant value of $k_z = 4\ \text{cm}^{-1}$.

Wavenumber components in $k_r < 0$ scan								
$k_\perp$ (cm^{-1})	4.5	6.5	10	15	20	28	36	45
$k_\perp\rho_s^{\text{exp}}$	3.1	4.6	7	10.5	14	19.6	25.2	31.5
k_R (cm^{-1})	−0.46	−4.74	−8.97	−14.35	−19.52	−27.67	−35.75	−44.80
k_Z (cm^{-1})	4	4	4	4	4	4	4	4
k_φ (cm^{-1})	−2.01	−1.94	−1.86	−1.77	−1.68	−1.53	−1.39	−1.23
$k_r\rho_s$	−0.06	−0.65	−1.24	−2.00	−2.72	−3.86	−4.99	−6.25
$k_\theta\rho_s$	5.17	4.91	4.66	4.34	4.03	3.54	3.06	2.52

TABLE IV. The set of wavenumber components used for scanning the $k_r > 0$ dependence of the spectrum in Sec. IV. All $\vec{k}_+$ have a constant value of $k_z = 4\,\text{cm}^{-1}$.

Wavenumber components in $k_r > 0$ scan								
$k_\perp$ (cm^{-1})	4.5	6.5	10	15	20	28	36	45
$k_\perp \rho_s^{exp}$	3.1	4.6	7	10.5	14	19.6	25.2	31.5
k_R (cm^{-1})	0.39	4.67	8.90	14.28	19.45	27.60	35.68	44.73
k_Z (cm^{-1})	4	4	4	4	4	4	4	4
k_φ (cm^{-1})	−2.03	−2.10	−2.17	−2.27	−2.36	−2.50	−2.64	−2.80
$k_r \rho_s$	0.06	0.66	1.25	2.00	2.73	3.87	5.00	6.26
$k_\theta \rho_s$	5.22	5.47	5.73	6.05	6.36	6.84	7.32	7.87

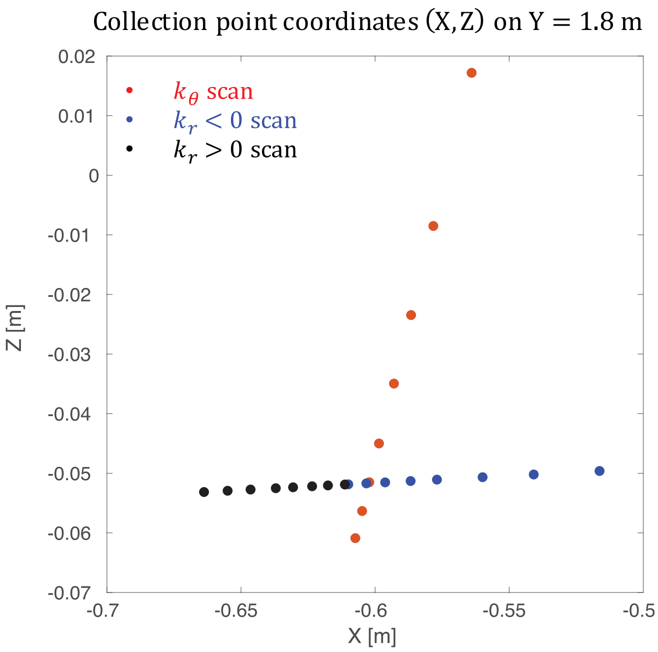

FIG. 14. Collection point coordinates (X, Z) taken to be at $Y = 1.8$ m for the different schemes developed in Sec. IV to scan the k_θ and k_r dependence of the high-k density spectrum. The Cartesian (X, Y, Z) coordinates are the same as in Fig. 9.

TABLE V. The sensitivity scans performed using electron-scale simulation for the strong ETG case are summarizing, including the value of the drive terms scanned ($a/L_{Te}, a/L_{ne}, q, \hat{s}$) used in the input, as well as the predicted value of the electron thermal power with respect to the experimental level P_e^{sim}/P_e^{exp}. The scaled parameter values with respect to the nominal, base case are shown in bold gray.

	Base	$\sigma(\nabla T, \nabla n)$	$\sigma(\nabla T)$ $q, \hat{s}$	$\sigma(\nabla n)$, $q, \hat{s}$	$\sigma(\nabla T, \nabla n)$, $q, \hat{s}$
$\mathbf{a/L_{Te}}$	3.3626	**4.2032**	**4.2032**	3.3626	**4.2032**
$\mathbf{a/L_{ne}}$	1.0048	**0.5024**	1.0048	**0.5024**	**0.5024**
q	3.7892	3.7892	**3.4103**	**3.4103**	**3.4103**
$\hat{\mathbf{s}}$	1.8047	1.8047	**2.1656**	**2.1656**	**2.1656**
$\mathbf{P_e^{sim}/P_e^{exp}}$	29%	70%	95%	91%	170%

comparisons with simulated spectra. This will prove useful to the gyrokinetic simulation expert and turbulence theoretician.

To end, in Fig. 14 are given the values of the collection point (X, Z) coordinates of the central scattered rays for each of the scans presented in Sec. IV. These could prove useful to understand the practical feasibility of the measurements as well as guide future experiments.

APPENDIX C: EXPERIMENTAL PLASMA PARAMETERS SCANNED

Table V summarizes the parametric scans performed for the five simulations corresponding to the strong ETG condition that were employed in the validation work of Sec. II C. The uncertainties in $a/L_{Te}, a/L_{ne}$ were computed from uncertainties in the background electron density and temperature profiles followed by a Monte Carlo analysis approach, and the values of $-10\%\, q$ and $+20\%\, \hat{s}$ were taken as reasonable estimates of the equilibrium reconstruction uncertainty.

REFERENCES

[1] B. Coppi, M. N. Rosenbluth, and R. Z. Sagdeev, Phys. Fluids **10**, 582 (1967).
[2] B. Kadomtsev and O. Pogutse, Nucl. Fusion **11**, 67 (1971).
[3] Y. C. Lee, J. Q. Dong, P. N. Guzdar, and C. S. Liu, Phys. Fluids **30**, 1331 (1987).
[4] W. Dorland, F. Jenko, M. Kotschenreuther, and B. N. Rogers, Phys. Rev. Lett. **85**, 5579 (2000).
[5] F. Jenko, W. Dorland, M. Kotschenreuther, and B. N. Rogers, Phys. Plasmas **7**, 1904 (2000).
[6] F. Jenko and W. Dorland, Phys. Rev. Lett. **89**, 225001 (2002).
[7] W. Horton, Rev. Mod. Phys. **71**, 735 (1999).
[8] M. Ono, S. M. Kaye, Y.-K. M. Peng, G. Barnes, W. Blanchard, M. D. Carter, J. Chrzanowski, L. Dudek, R. Ewig, D. Gates, R. E. Hatcher, T. Jarboe, S. C. Jardin, D. Johnson, R. Kaita, M. Kalish, C. E. Kessel, H. W. Kugel, R. Maingi, R. Majeski, J. Manickam, B. McCormack, J. Menard, D. Mueller, B. A. Nelson, B. E. Nelson, C. Neumeyer, G. Oliaro, F. Paoletti, R. Parsells, E. Perry, N. Pomphrey, S. Ramakrishnan, R. Raman, G. Rewoldt, J. Robinson, A. L. Roquemore, P. Ryan, S. Sabbagh, D. Swain, E. J. Synakowski, M. Viola, M. Williams, J. R. Wilson, and the NSTX Team, Nucl. Fusion **40**, 557 (2000).
[9] A. Sykes, the START Team, the NBI Team, the MAST Team, and Theory Team, Nucl. Fusion **39**, 1271 (1999).
[10] J. Candy and R. E. Waltz, J. Comput. Phys **186**, 545 (2003).
[11] W. Guttenfelder, J. L. Peterson, J. Candy, S. M. Kaye, Y. Ren, R. E. Bell, G. W. Hammett, B. P. LeBlanc, D. R. Mikkelsen, W. M. Nevins, and H. Yuh, Nucl. Fusion **53**, 093022 (2013).
[12] F. Jenko, W. Dorland, and G. W. Hammett, Phys. Plasmas **8**, 4096 (2001).
[13] R. D. Hazeltine and H. R. Strauss, Phys. Rev. Lett. **37**, 102 (1976).

Published under license by AIP Publishing

[14] J. F. Drake, N. T. Gladd, C. S. Liu, and C. L. Chang, Phys. Rev. Lett. **44**, 994 (1980).
[15] W. Guttenfelder, J. Candy, S. M. Kaye, W. M. Nevins, E. Wang, R. E. Bell, G. W. Hammett, B. P. LeBlanc, D. R. Mikkelsen, and H. Yuh, Phys. Rev. Lett. **106**, 155004 (2011).
[16] W. Tang, J. Connor, and R. Hastie, Nucl. Fusion **20**, 1439 (1980).
[17] J. R. Ruiz, Y. Ren, W. Guttenfelder, A. E. White, S. M. Kaye, B. P. Leblanc, E. Mazzucato, K. C. Lee, C. W. Domier, D. R. Smith, and H. Yuh, Phys. Plasmas **22**, 122501 (2015).
[18] J. R. Ruiz, W. Guttenfelder, A. E. White, N. T. Howard, J. Candy, Y. Ren, D. R. Smith, N. F. Loureiro, C. Holland, and C. W. Domier, Plasma Phys. Controlled Fusion **61**, 115015 (2019).
[19] J. R. Ruiz, W. Guttenfelder, A. E. White, N. T. Howard, J. Candy, Y. Ren, D. R. Smith, and C. Holland, Plasma Phys. Controlled Fusion **62**, 075001 (2020).
[20] Y. Ren, W. X. Wang, W. Guttenfelder, S. M. Kaye, J. Ruiz Ruiz, S. Ethier, R. Bell, B. P. Leblanc, E. Mazzucato, D. R. Smith, C. W. Domier, and H. Yuh, Nucl. Fusion **60**, 026005 (2020).
[21] D. R. Smith, E. Mazzucato, W. Lee, H. K. Park, C. W. Domier, and N. C. Luhmann, Jr., Rev. Sci. Instrum. **79**, 123501 (2008).
[22] R. J. Hawryluk, *Physics of Plasma Close to Thermonuclear Conditions* (Pergamon, New York, 1981).
[23] E. A. Belli and J. Candy, Plasma Phys. Controlled Fusion **50**, 095010 (2008).
[24] J. Candy and E. Belli, *GYRO Technical Guide* (General Atomics, San Diego, 2014.).
[25] J. Candy, E. A. Belli, and R. V. Bravenec, J. Comput. Phys. **324**, 73–93 (2016).
[26] R. L. Miller, M. S. Chu, J. M. Greene, Y. R. Lin-Liu, and R. E. Waltz, Phys. Plasmas **5**, 973 (1998).
[27] R. Barchfeld, C. W. Domier, Y. Ren, R. Ellis, P. Riemenschneider, N. Allen, R. Kaita, B. Stratton, J. Dannenberg, Y. Zhu, and N. C. Luhman, Jr., Rev. Sci. Instrum. **89**, 10C114 (2018).
[28] Y. Ren, E. Belova, N. Gorelenkov, W. Guttenfelder, S. M. Kaye, E. Mazzucato, J. L. Peterson, D. R. Smith, D. Stutman, K. Tritz, W. X. Wang, H. Yuh, C. W. Domier, and B. P. LeBlanc, Nucl. Fusion **57**, 072002 (2017).
[29] A. M. Dimits, G. Bateman, M. A. Beer, B. I. Cohen, W. Dorland, G. W. Hammett, C. Kim, J. E. Kinsey, M. Kotschenreuther, A. H. Kritz, L. L. Lao, J. Mandrekas, W. M. Nevins, S. E. Parker, A. J. Redd, D. E. Shumaker, R. Sydora, and J. Weiland, Phys. Plasmas **7**, 969 (2000).
[30] F. van Wyk, E. G. Highcock, A. A. Schekochihin, C. M. Roach, A. R. Field, and W. Dorland, J. Plasma Phys. **82**, 905820609 (2016).
[31] M. N. Rosenbluth and F. L. Hinton, Phys. Rev. Lett. **80**, 724 (1998).
[32] F. L. Hinton and M. N. Rosenbluth, Plasma Phys. Controlled Fusion **41**, A653 (1999).
[33] Z. Lin, T. S. Hahm, W. W. Lee, W. M. Tang, and P. H. Diamond, Phys. Rev. Lett. **83**, 3645 (1999).
[34] E. A. Belli and J. Candy, Plasma Phys. Controlled Fusion **59**, 045005 (2017).
[35] E. Mazzucato, Phys. Rev. Lett. **36**, 792 (1976).
[36] C. M. Surko and R. E. Slusher, Phys. Rev. Lett. **37**, 1747 (1976).
[37] W. A. Peebles, N. C. Luhmann, Jr., A. Mase, H. Park, and A. Semet, Rev. Sci. Instrum. **52**, 360 (1981).
[38] R. E. Slusher and C. M. Surko, Phys. Fluids **23**, 472 (1980).
[39] H. Park, C. X. Yu, W. A. Peebles, N. C. Luhmann, Jr., and R. Savage, Rev. Sci. Instrum. **53**, 1535 (1982).
[40] P. Devynck, X. Garbet, C. Laviron, J. Payan, S. K. Saha, F. Gervais, P. Hennequin, A. Quemeneur, and A. Truc, Plasma Phys. Controlled Fusion **35**, 63 (1993).
[41] E. Mazzucato, Phys. Plasmas **10**, 753 (2003).
[42] E. Mazzucato, Plasma Phys. Controlled Fusion **48**, 1749 (2006).
[43] Y. Ren, private communication, 2020.
[44] C. Holland, A. E. White, G. R. McKee, M. W. Shafer, J. Candy, R. E. Waltz, L. Schmitz, and G. R. Tynan, Phys. Plasmas **16**, 052301 (2009).
[45] C. Holland, J. C. DeBoo, T. L. Rhodes, L. Schmitz, J. C. Hillesheim, G. Wang, A. E. White, M. E. Austin, E. J. Doyle, W. A. Peebles, C. C. Petty, L. Zeng, and J. Candy, Nucl. Fusion **52**, 063028 (2012).
[46] F. M. Poli, S. Ethier, W. Wang, T. S. Hahm, E. Mazzucato, and D. R. Smith, Phys. Plasmas **17**, 112514 (2010).
[47] F. I. Parra, M. Barnes, and A. G. Peeters, Phys. Plasmas **18**, 062501 (2011).
[48] M. F. J. Fox, F. van Wyk, A. R. Field, Y.-c. Ghim, F. I. Parra, and A. A. Schekochihin, and the MAST Team, Plasma Phys. Controlled Fusion **59**, 034002 (2017).
[49] W. Guttenfelder and J. Candy, Phys. Plasmas **18**, 022506 (2011).
[50] C. M. Roach, I. G. Abel, R. J. Akers, W. Arter, M. Barnes, Y. Camenen, F. J. Casson, G. Colyer, J. W. Connor, S. C. Cowley, D. Dickinson, W. Dorland, A. R. Field, W. Guttenfelder, G. W. Hammett, R. J. Hastie, E. Highcock, N. F. Loureiro, A. G. Peeters, M. Reshko, S. Saarelma, A. A. Schekochihin, M. Valovic, and H. R. Wilson, Plasma Phys. Controlled Fusion, Fusion **51**, 124020 (2009).
[51] N. T. Howard, C. Holland, A. E. White, M. Greenwald, and J. Candy, Nucl. Fusion **56**, 014004 (2016).
[52] P. W. Terry, M. Greenwald, J.-N. Leboeuf, G. R. McKee, D. R. Mikkelsen, W. M. Nevins, D. E. Newman, and D. P. Stotler, "Task Group on Verification and Validation, U.S. Burning Plasma Organization, and U.S. Transport Task Force," Phys. Plasmas **15**, 062503 (2008).
[53] M. Greenwald, Phys. Plasmas **17**, 058101 (2010).
[54] P. Ricci, C. Theiler, A. Fasoli, I. Furno, K. Gustafson, D. Iraji, and J. Loizu, Phys. Plasmas **18**, 032109 (2011).
[55] C. Holland, Phys. Plasmas **23**, 060901 (2016).
[56] G. M. Staebler, J. M. Kinsey, and R. E. Waltz, Phys. Plasmas **12**, 102508 (2005).

Published under license by AIP Publishing